

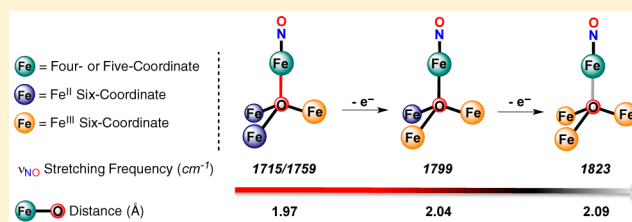
Nitric Oxide Activation by Distal Redox Modulation in Tetranuclear Iron Nitrosyl Complexes

Graham de Ruiter, Niklas B. Thompson, Davide Lionetti, and Theodor Agapie*

Division of Chemistry and Chemical Engineering, California Institute of Technology, Pasadena, California 91125, United States

S Supporting Information

ABSTRACT: A series of tetranuclear iron complexes displaying a site-differentiated metal center was synthesized. Three of the metal centers are coordinated to our previously reported ligand, based on a 1,3,5-triarylbenzene motif with nitrogen and oxygen donors. The fourth (apical) iron center is coordinatively unsaturated and appended to the trinuclear core through three bridging pyrazolates and an interstitial μ_4 -oxide moiety. Electrochemical studies of complex $[\text{LFe}_3(\text{PhPz})_3\text{OFe}][\text{OTf}]_2$ revealed three reversible redox events assigned to the $\text{Fe}^{\text{II}}_4/\text{Fe}^{\text{II}}_3\text{Fe}^{\text{III}}$ (-1.733 V), $\text{Fe}^{\text{II}}_2\text{Fe}^{\text{III}}/\text{Fe}^{\text{II}}_2\text{Fe}^{\text{III}}_2$ (-0.727 V), and $\text{Fe}^{\text{II}}_2\text{Fe}^{\text{III}}_2/\text{Fe}^{\text{II}}\text{Fe}^{\text{III}}_3$ (0.018 V) redox couples. Combined Mössbauer and crystallographic studies indicate that the change in oxidation state is exclusively localized at the triiron core, without changing the oxidation state of the apical metal center. This phenomenon is assigned to differences in the coordination environment of the two metal sites and provides a strategy for storing electron and hole equivalents without affecting the oxidation state of the coordinatively unsaturated metal. The presence of a ligand-binding site allowed the effect of redox modulation on nitric oxide activation by an Fe^{II} metal center to be studied. Treatment of the clusters with nitric oxide resulted in binding of NO to the apical iron center, generating a $\{\text{FeNO}\}^7$ moiety. As with the NO-free precursors, the three reversible redox events are localized at the iron centers distal from the NO ligand. Altering the redox state of the triiron core resulted in significant change in the NO stretching frequency, by as much as 100 cm^{-1} . The increased activation of NO is attributed to structural changes within the clusters, in particular, those related to the interaction of the metal centers with the interstitial atom. The differences in NO activation were further shown to lead to differential reactivity, with NO disproportionation and N_2O formation performed by the more electron-rich cluster.



INTRODUCTION

Challenging chemical transformations involving the transfer of multiple electrons and protons are commonly catalyzed in living organisms by proteins that display multiple metals in the active site.¹ One such example is the oxidation of H_2O to O_2 by the oxygen-evolving complex (OEC) in photosystem II (PSII).^{1d,2} The active site consists of a mixed manganese–calcium cubane $[\text{Mn}_4\text{CaO}_n]$,^{1d,2,3} which cycles through five oxidation states upon photoexcitation (S-states).⁴ These successive oxidations culminate in the oxidation of water with subsequent release of dioxygen.^{1d,2–4} Other proteins that feature multinuclear active sites include hydrogenase,⁵ CO dehydrogenase,⁶ laccase,^{1c,7} acetyl-CoA synthase,⁸ Cytochrome c oxidase,⁹ and nitrogenase.^{1a,10} Although Mn features preeminently as a example of biological multielectron catalysis, Fe is encountered in most other multinuclear active sites mentioned above for the reduction of H_2O to H_2 , of CO_2 to CO , of N_2 to NH_3 , and of O_2 to H_2O . The nitrogenase enzyme family is notable for the number of electrons (six) required for the transformation of N_2 to NH_3 and for the number of metals centers (eight) present in the active site, with seven of them being iron in all isoforms.^{1a,10d,11} The presence of multimetallic active sites has inspired mechanistic proposals that invoke metal–metal cooperativity in substrate activation^{6–10} or

product formation.^{2–4} The ability to store multiple redox equivalents and to tune reduction potentials has also been explored for multimetallic active sites.^{1d,10a,12} When the proposed site of substrate binding consists of a single metal within a multimetallic assembly, the other noncoordinating metals have been, in some cases, speculated to alter the geometry of the bridging ligands or influence the electronics of the multimetallic assembly in order to affect substrate conversion.^{1g,8} Despite a wealth of studies, the respective mechanisms of several multimetallic active sites remain under debate.

Investigating the roles that these metals play in multimetallic active sites is important for understanding their contribution to (i) substrate binding and activation, (ii) redox tuning, (iii) storage of redox equivalents, or (iv) electron shuttling. Such investigation is instrumental for obtaining a detailed mechanistic picture and for rational design of artificial catalysts. Modeling chemistry has been challenging due to the complexity of multimetallic targets.

Our group and others have targeted metal complexes that, conceptually, help to understand the various aspects involved in

Received: July 15, 2015

Published: September 21, 2015

the functioning of the active sites of a wide variety of enzymes.¹³ We have studied the effects of redox-inactive metals as part of redox-active transition metal clusters, a topic of interest in the context of the role of calcium in the OEC.^{12,14} Access to hetero- and homonuclear clusters was achieved rationally via a stepwise route starting from trinuclear precursors.¹⁵ It was demonstrated that the redox potential of these metal cluster correlates linearly with the Lewis acidity of the fourth redox-inactive or redox-active metal, providing a strategy for redox tuning of the cluster.¹² A related question concerns the effect of redox-active metals on reactivity, in particular, the effect of oxidation state changes on small molecule activation at a remote positions in the cluster. To address this question, we designed a new class of metal clusters that display multiple, reversible redox events and that are site-differentiated to allow for separation of the location of redox changes and small molecule binding (Figure 1).

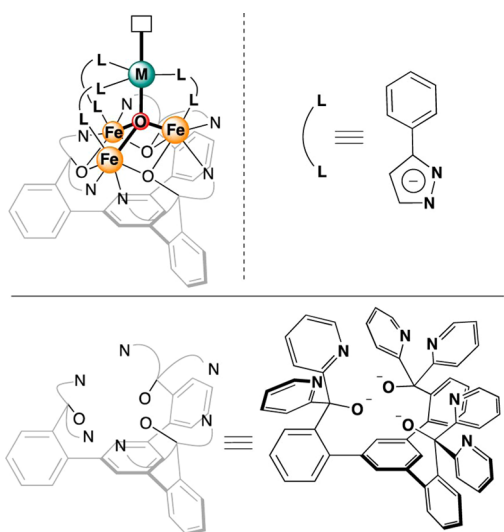


Figure 1. General molecular structure of tetranuclear clusters (top left) reported, supported by pyrazolates (top right) and a 1,3,5-triarylbenzene-based ligand (bottom).

Herein, we present the synthesis of site-differentiated tetranuclear iron clusters. The apical metal site (green) is four-coordinate, with a trigonal pyramidal geometry prone to bind a variety of small molecules.¹⁶ The “bottom” metal sites (orange) are coordinatively saturated and are known to undergo redox changes in related clusters.^{12b} The four-coordinate apical iron center is sufficiently different that electron transfer processes are localized at the triiron core. Exposing the metal clusters to nitric oxide (NO) results in coordination of NO to the apical iron center in three of the four redox states of the cluster. With the apical metal maintaining the same oxidation state, the effect of distal redox changes on NO activation was investigated based on variation of the NO stretching frequency. The changes in ν_{NO} , as high as 100 cm^{-1} , demonstrate that remote redox changes can have a significant influence on small molecules bound to the cluster. The mechanism of redox modulation is discussed, and their effect on chemical reactivity is investigated.

RESULTS AND DISCUSSION

Given the precedent for small molecule activation at metal centers supported by equatorial nitrogen donors,^{16a,d-g,i-1} we

sought to synthesize tetranuclear iron clusters, with pyrazolates as bridging ligands, to generate a trigonal pyramidal environment around the apical metal. Starting from the recently reported triiron precursor $\text{LFe}_3(\text{OAc})_3$ (**1**),^{15a} one-pot procedures proved to be unsuccessful at installing all three pyrazolate donors, most likely due to the strong binding of the three acetates to the triiron core. Less coordinating anions were envisioned to result in a more reactive precursor. Treatment of **1** with excess MeOTf (OTf = trifluoromethanesulfonate) leads to the formation of a new species according to the ^1H NMR spectrum (Figure S3). Even though an excess of MeOTf was used, subsequent reactivity suggests the presence of some acetate anion. This species was thus assigned as having a stoichiometry of $\text{LFe}_3(\text{OTf})_2(\text{OAc})$, although elemental analysis is indicative of complete substitution of acetate with triflates.

Addition of a slight excess of sodium phenylpyrazolate (3.3 equiv) to $\text{LFe}_3(\text{OTf})_2(\text{OAc})$ followed by treatment with iodobenzene (PhIO, 1.0 equiv) resulted in the formation of a new species with a ^1H NMR spectrum that is paramagnetically shifted over 100 ppm (Figure S4). Electrospray ionization mass spectrometry (ESI-MS) analysis of an aliquot taken from the crude reaction mixture shows a peak at $m/z = 1491.0$, consistent with the *in situ* formation of $[\text{LFe}_3(\text{PhPz})_3\text{ONa}][\text{OTf}]$ (Figure S5; $m/z = 1491.3$, PhPz = 3-phenylpyrazolate). Addition of $\text{Fe}(\text{OTf})_2$ (2.0 equiv) to this reaction mixture yielded the tetranuclear complex $[\text{LFe}_3(\text{PhPz})_3\text{OFe}][\text{OTf}]_2$ (**4**) in ~50% isolated yield. Although these, and subsequently reported complexes, are paramagnetic, the ^1H NMR spectra display characteristic resonances that allow facile identification of the parent complexes (Figures S6–S8 and S17–S19).

Crystals of **4**, suitable for single-crystal X-ray diffraction (XRD), were grown by vapor diffusion of diethyl ether into a concentrated solution of **4** in acetonitrile. Complex **4** features a single dication in the asymmetric unit, with two outer-sphere triflates (Figure 2). The coordination environment around the apical iron metal center (Fe4) is trigonal pyramidal, with the three pyrazolate nitrogen donors (N14, N24, and N34) forming a trigonal plane (Figures 2 and 4A). The Fe4–N_{pz} bond distances range from 2.065(4) to 2.095(4) Å, with near identical Fe–N–N angles (Table 1). The apical iron center is connected to the triiron core through a μ_4 -oxide moiety (O1), resulting in a $[\text{Fe}_4(\mu_4\text{-O})]$ core. The Fe1–O1, Fe2–O1, and Fe3–O1 bond distances of 2.069(2), 1.998(2), and 1.932(2) Å, respectively, are indicative of a $[\text{Fe}^{\text{II}}\text{Fe}^{\text{III}}_2]$ triiron core (Table 1). These observations are consistent with other tetrametallic complexes, where reduction of a triiron core ($\text{Fe}^{\text{III}}_3 \rightarrow \text{Fe}^{\text{II}}\text{Fe}^{\text{III}}_2$) resulted in the lengthening of one of the Fe–O1 bond distances.^{12b} Together with the presence of two outer-sphere triflates, the formal oxidation state of the complex is thus assigned as $[\text{LFe}^{\text{II}}\text{Fe}^{\text{III}}_2(\text{PhPz})_3\text{OFe}^{\text{II}}]^{2+}$. The presence of a μ_4 -oxido is a common bridging motif in variety of reported clusters, and the presence of a $[\text{Fe}_4(\mu_4\text{-O})]$ core has been described in the literature as a part of numerous polynuclear complexes ($M > 4$).^{17,18} In contrast, to the best of our knowledge, the presence of a discrete of $[\text{Fe}_4(\mu_4\text{-O})]$ core is quite rare. To date, only a handful of complexes have been reported that feature such a moiety.^{17c,18,19}

In order to test the accessibility of other redox states of this cluster, the electrochemical properties of **4** were investigated by cyclic voltammetry (CV). The CV of complex **4** (Figure 3) displays three reversible one-electron redox-events at -1.733 , -0.727 , and 0.018 V (vs Fc/Fc^+). These oxidation/reduction

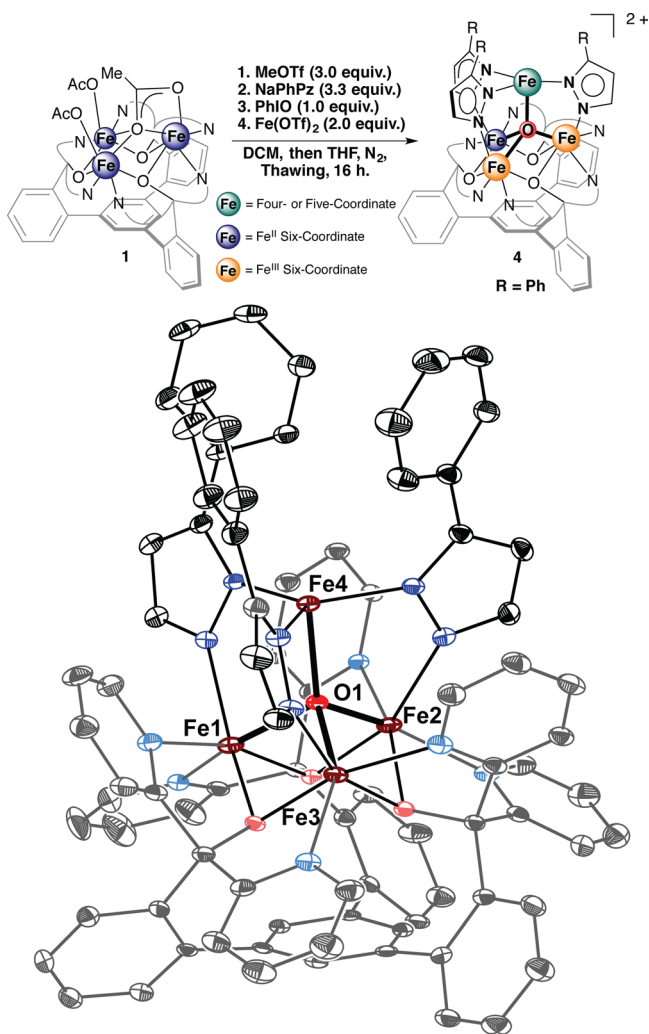


Figure 2. Synthesis (top) and crystal structure (bottom) of tetranuclear complex $[\text{LFe}_3(\text{PhPz})_3\text{OFe}][\text{OTf}]_2$ (**4**). Solvents, outer-sphere counterions, and hydrogen atoms are omitted for clarity. Thermal ellipsoids are shown at the 50% probability level.

waves are assigned to the $\text{Fe}^{\text{II}}_4/\text{Fe}^{\text{II}}_3\text{Fe}^{\text{III}}$ (-1.733 V), $\text{Fe}^{\text{II}}_3\text{Fe}^{\text{III}}/\text{Fe}^{\text{II}}_2\text{Fe}^{\text{III}}_2$ (-0.727 V), and $\text{Fe}^{\text{II}}_2\text{Fe}^{\text{III}}_2/\text{Fe}^{\text{II}}\text{Fe}^{\text{III}}_3$ (0.018 V) redox couples. Interestingly, the oxidation from Fe^{II} to Fe^{III} of the fourth iron center is not observed, even at a potential of $+1.0$ V vs Fc/Fc^+ . The large number of accessible redox states in **4** is nonetheless notable for tetranuclear clusters.

Until now, a discrete $[\text{Fe}_4(\mu_4\text{-O})]$ core capable of supporting four oxidation states has not yet been reported. Even in biology, where iron–sulfur clusters can exist in several oxidation states, they usually utilize only a single redox couple, as shown by ferredoxins and high potential iron–sulfur proteins.²⁰ Synthetic iron–sulfur clusters are known to access multiple oxidation states.^{20,21} Hexanuclear complexes with multiple reversible metal-based redox events (≥ 3) have been reported as well.²² For example, a hexanuclear iron cluster has been shown to support up to five redox events spanning a potential window of only 1.3 V.^{22a,b} Recently reported bimetallic complexes of first-row transition metals exhibited multiple redox events as well, in contrast to their monometallic counterparts.²³ Other notable examples include mononuclear complexes of the type $[\text{M}(\text{bpy})_3]^n$ ($n = 3^+$, 2^+ , 1^+ , 1^- , 2^- , and 3^-), although, in these cases, many of the redox events are ligand-based.²⁴

Having established the electrochemical properties of complex **4**, attempts were made to chemically oxidize/reduce it in order to isolate the putative complexes $[\text{LFe}_3(\text{PhPz})_3\text{OFe}]$ (**2**), $[\text{LFe}_3(\text{PhPz})_3\text{OFe}][\text{OTf}]$ (**3**), and $[\text{LFe}_3(\text{PhPz})_3\text{OFe}][\text{OTf}]_3$ (**5**). Reduction of complex **4** with 1.0 equiv of cobaltocene (CoCp_2) in CH_2Cl_2 for 2 h resulted in a color change from yellow-brown to red-purple. The ^1H NMR spectrum changes significantly and is indicative of the formation of a new paramagnetic species (Figure S7). This species was identified as the one-electron-reduced $[\text{LFe}_3(\text{PhPz})_3\text{OFe}][\text{OTf}]$ (**3**, $\text{PhPz} = 3\text{-phenylpyrazolate}$) by XRD (Scheme 1 and Figure S32). Conversely, treatment of complex **4** with 1.0 equiv of silver triflate (AgOTf) in CH_2Cl_2 for 2 h resulted in a paramagnetic species different from **3** or **4** (Figure S8). This new complex, **5**, was identified by XRD as the one-electron-oxidized $\text{LFe}_3(\text{PhPz})_3\text{OFe}][\text{OTf}]_3$ (Scheme 1 and Figure S34). On the basis of our electrochemical studies, further reduction of complex **3** should be possible ($\text{Fe}^{\text{II}}_4/\text{Fe}^{\text{II}}_3\text{Fe}^{\text{III}}$ at -1.733 V). Indeed, treating **3** with 1.0 equiv of dexamethylcobaltocene (CoCp^{*2}) in THF resulted in the formation of a blue precipitate that is insoluble in common organic solvents including DMF, MeCN, THF, DME, toluene, ether, and hexanes, among others. The insolubility precluded us from obtaining a solution ^1H NMR spectrum and X-ray quality crystals. However, further reactivity studies are consistent with reduction of the same cluster core, leading to an assignment of $[\text{LFe}_3(\text{PhPz})_3\text{OFe}]$ (Scheme 1 and Figures S9–S11).

Definite structural assignments for complexes **3** and **5** were made on the basis of XRD. For crystallographic purposes, complex **3** was crystallized as the corresponding tetrafluoroborate (BF_4^-) salt (Figures S12 and S32). In complexes **3** and **5**, the coordination environment around the apical iron metal center (Fe4) is trigonal pyramidal, analogous to complex **4**. The three pyrazolate nitrogen donors (N14 , N24 , and N34) form a trigonal plane with nearly identical $\text{Fe4}-\text{N}_{\text{pz}}$ bond distances irrespective of oxidation state (Figures S32–S34 and Table 1). The apical iron center is appended to the triiron core through a μ_4 -oxido (O1), as in complex **4**. Analysis of the structural parameters indicates that sequential oxidation of complex **3** to **4** and **5** leads to significant elongation of the $\text{Fe4}-\text{O1}$ bond distances: **3**, $1.908(3)$ Å; **4**, $1.971(2)$ Å; **5**, $2.031(2)$ Å (Figure 4A–D). This trend is correlated with a decrease in the $[\text{Fe1}|\text{Fe2}|\text{Fe3}]$ centroid– O1 distance from 0.969 Å in **3** to 0.888 Å in **5** (Table 1). These changes are attributed to the increase in Lewis acid character of the triiron core upon oxidation, which leads to a stronger interaction with O1 . In agreement, oxidation results in contraction of the $\text{Fe1}-\text{N13}$, $\text{Fe2}-\text{N23}$, and $\text{Fe3}-\text{N33}$ bond distances.

Other structural changes are found in the $[\text{Fe}_4(\mu_4\text{-O})]$ core, which are dependent on the oxidation state of the metal centers (Figure 4A–D and Table 1).^{12b,c} For instance, in complex **3**, the $\text{Fe1}-\text{O1}$ and $\text{Fe2}-\text{O1}$ distances ($2.073(3)$ and $2.088(3)$ Å, respectively) are longer than $\text{Fe3}-\text{O1}$ ($1.894(3)$ Å), indicative of Fe^{II} centers at the Fe1 and Fe2 positions and Fe^{III} for Fe3 . These bond distances are consistent with an $[\text{Fe}^{\text{II}}_2\text{Fe}^{\text{III}}]$ oxidation state of the triiron core^{12b} and are in line with our electrochemical and spectroscopic studies (*vide supra*). The one-electron oxidation of complex **3** leads to a considerable contraction of the $\text{Fe2}-\text{O1}$ distance from $2.088(3)$ Å in complex **3** to $1.998(2)$ in complex **4** (Figure 4C). Similarly, in complex **5**, the $\text{Fe1}-\text{O1}$, $\text{Fe2}-\text{O1}$, and $\text{Fe3}-\text{O1}$ distances are nearly identical, consistent with a $[\text{Fe}^{\text{III}}_3]$ core in complex **5** (Figure 4D). The change in bond distances thus indicate that

Table 1. Selected Bond Angles and Distances for Complexes 3–8

bond distance (Å)	complex					
	3	4	5	6	7	8
Fe1–O1	2.073(3)	2.069(2)	1.984(2)	2.113(2)	2.184(3)	1.979(5)
Fe2–O1	2.088(3)	1.998(2)	1.966(2)	2.070(2)	1.928(3)	1.995(5)
Fe3–O1	1.894(3)	1.932(2)	1.976(2)	1.952(2)	1.944(3)	2.004(5)
Fe4–O1	1.908(3)	1.971(2)	2.031(2)	1.968(2)	2.035(3)	2.087(5)
Fe1–N13	2.146(4)	2.120(2)	2.057(2)	2.134(3)	2.103(3)	2.065(6)
Fe2–N23	2.161(3)	2.111(3)	2.060(3)	2.117(3)	2.091(3)	2.033(6)
Fe3–N33	2.130(4)	2.083(3)	2.054(3)	2.129(3)	2.073(3)	2.040(7)
Fe4–N14	2.065(4)	2.046(3)	2.048(3)	2.124(3)	2.054(3)	2.068(6)
Fe4–N24	2.067(4)	2.065(3)	2.061(3)	2.068(3)	2.098(3)	2.082(7)
Fe4–N34	2.095(4)	2.064(3)	2.054(3)	2.108(3)	2.081(3)	2.062(7)
N13–N14	1.387(5)	1.387(4)	1.388(3)	1.382(3)	1.378(5)	1.358(9)
N23–N24	1.387(5)	1.392(4)	1.380(4)	1.381(3)	1.276(5)	1.387(9)
N33–N34	1.390(5)	1.390(4)	1.383(3)	1.384(2)	1.380(5)	1.38(1)
Fe4–N40				1.774(3)	1.772(4)	1.763(7)
N40–O40				1.157(3)	1.144(5)	1.144(8)
bond angles (deg)						
N14–Fe4–N24	119.92(15)	119.12(11)	119.35(10)	118.1(1)	117.4(1)	119.1(3)
N24–Fe4–N34	119.06(14)	120.13(11)	118.00(10)	115.7(1)	126.0(1)	120.3(3)
N34–Fe4–N14	120.27(14)	120.66(11)	122.37(10)	124.5(1)	114.3(1)	115.9(3)
O1–Fe4–N40				175.6(1)	175.9(1)	177.8(3)
Fe4–N40–O40				169.6(3)	171.4(4)	171.9(7)
torsion angles (deg)						
Fe1–N13–N14–Fe4	–2.1(4)	3.8(3)	1.5(3)	15.4(3)	–20.4(4)	31.9(6)
Fe2–N23–N24–Fe4	–3.2(4)	–1.4(3)	–2.7(3)	17.6(3)	12.9(4)	21.5(7)
Fe3–N33–N34–Fe4	–1.6(4)	–1.1(3)	1.1(3)	28.9(3)	27.8(4)	20.1(9)
centroid distances (Å)						
Fe1 Fe2 Fe3–N14 N24 N34	2.973	2.947	2.870	2.862	2.811	2.750
Fe1 Fe2 Fe3–O11 O21 O31	1.069	1.086	1.083	1.092	1.085	1.058
Fe1 Fe2 Fe3–O1	0.969	0.943	0.888	1.057	0.999	0.921
N14 N24 N34–Fe4	0.105	0.037	0.059	0.166	0.222	0.260

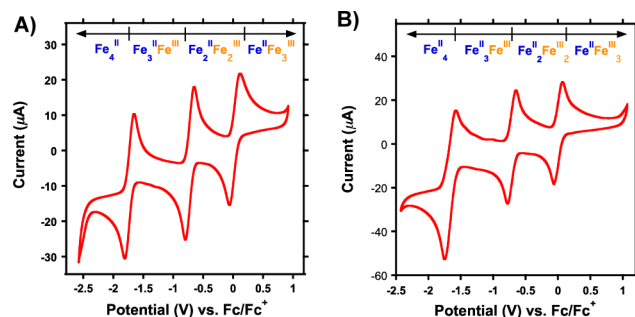


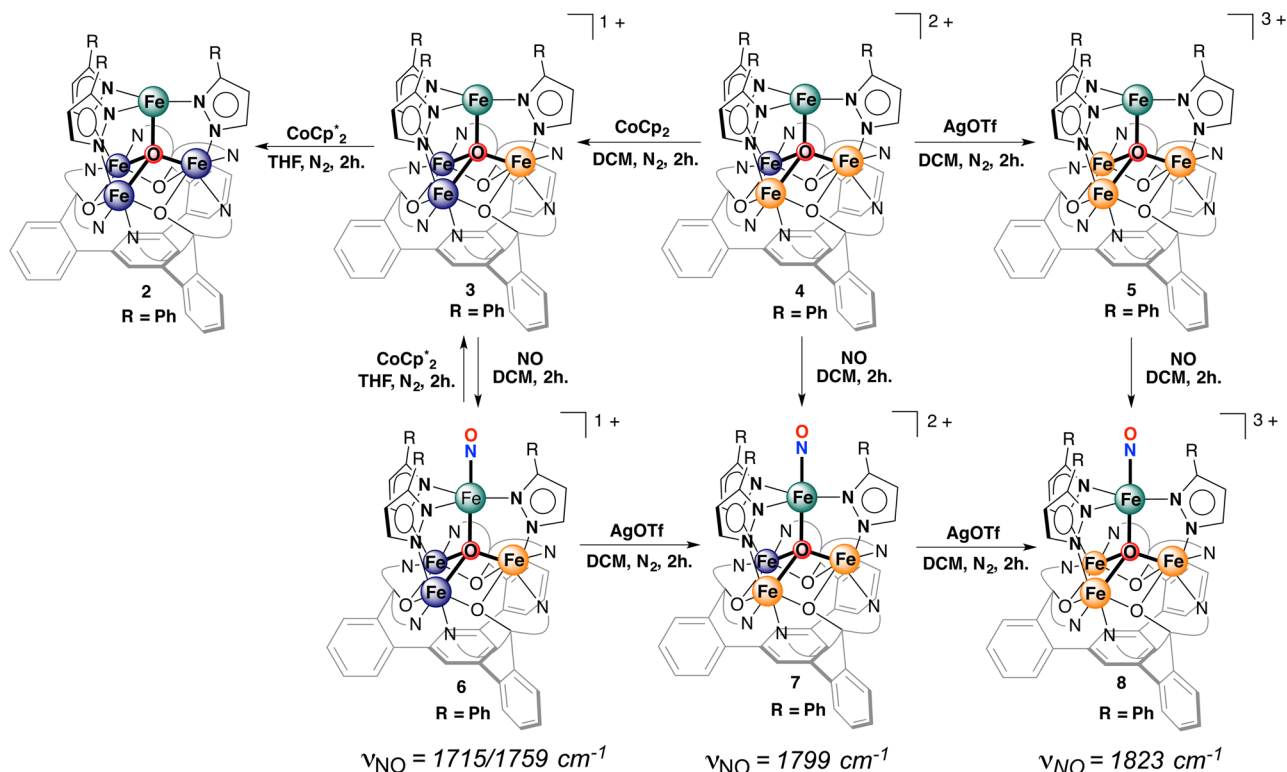
Figure 3. Cyclic voltammograms (CVs) of $[\text{LFe}_3(\text{PhPz})_3\text{OFe}][\text{OTf}]_2$ (A) and $[\text{LFe}_3(\text{PhPz})_3\text{OFeNO}][\text{OTf}]_2$ (B) at a scan rate of 100 mV s^{-1} . CVs were recorded in CH_2Cl_2 at a concentration of 2 mM , with glassy carbon, Pt-wire, and Ag-wire as the working, counter, and reference electrodes, respectively. $n\text{Bu}_4\text{NPF}_6$ (0.1 M) was used as the supporting electrolyte. The measured open-circuit potential (OCP) was ca. 0.0 V for both complexes.

the triiron core shuttles between oxidation states: $[\text{Fe}^{\text{II}}_3] \rightleftharpoons [\text{Fe}^{\text{II}}_2\text{Fe}^{\text{III}}] \rightleftharpoons [\text{Fe}^{\text{II}}\text{Fe}^{\text{III}}_2] \rightleftharpoons [\text{Fe}^{\text{III}}_3]$. Consequently, the redox waves at -1.733 , -0.727 , and 0.018 V are assigned to redox events localized at the triiron core

The changes in redox state of the iron metal centers were further investigated using zero-field ^{57}Fe Mössbauer spectroscopy (Figures 4E–G and Table 2). The Mössbauer spectrum of complex 3 displays broad features that are best modeled as four quadrupole doublets in a 1:1:1:1 ratio, consistent with the

presence for four inequivalent iron metal centers (Figure 4E). The nearly identical quadrupole doublets with isomer shifts of $\delta = 1.121$ (dashed blue trace) and 1.128 (solid blue trace) mm/s , with quadrupole splitting of $|\Delta E_Q| = 3.172$ and 3.569 mm/s , respectively, are indicative of the presence of two high-spin ferrous ions.²⁵ The assignment of the redox states in the triiron core as $[\text{Fe}^{\text{II}}_2\text{Fe}^{\text{III}}]$ is completed by assigning the isomer shift at $\delta = 0.452 \text{ mm/s}$ (solid orange trace) with a quadrupole splitting of $|\Delta E_Q| = 1.188 \text{ mm/s}$ as a high-spin ferric center.²⁵ Metal clusters featuring a nearly identical $[\text{Fe}_4(\mu_4\text{O})]$ core exhibit similar Mössbauer parameters for high-spin Fe centers.^{18,19b} Overall, the observed Mössbauer parameters are in-line with those of other six-coordinate $\text{Fe}^{\text{II}}/\text{Fe}^{\text{III}}$ centers bearing N- and O-donor atoms²⁶ and are nearly identical to those observed for the $[\text{Fe}^{\text{II}}_2\text{Fe}^{\text{III}}]$ triiron core in our previously reported oxido/hydroxido scandium complex.^{12b} The remaining quadrupole doublet at $\delta = 0.953$ (solid green trace) with a quadrupole splitting of $|\Delta E_Q| = 2.074 \text{ mm/s}$ is indicative of a high-spin Fe^{II} metal center in a four-coordinate geometry and is assigned to the apical Fe center.²⁷

With the Mössbauer spectrum of 3 assigned as $[\text{LFe}^{\text{II}}_2\text{Fe}^{\text{III}}(\text{PhPz})_3\text{OFe}^{\text{II}}]$, the elucidation of oxidation states in complexes 4 and 5 is facile, given the similarities in the Mössbauer parameters (Figure 4E,G and Table 2). The Mössbauer spectrum of complex 4, compared to 3, shows a major difference in the shift of the quadrupole doublet at $\delta = 1.121 \text{ mm/s}$ (Figure 4E, dashed blue trace) to $\delta = 0.431 \text{ mm/s}$,

Scheme 1. Synthesis of Tetrairon Complexes 2–8^a

^aThe oxidation states of the iron metal centers are highlighted in blue (Fe^{II}) and orange (Fe^{III}). The apical metal center is highlighted in green.

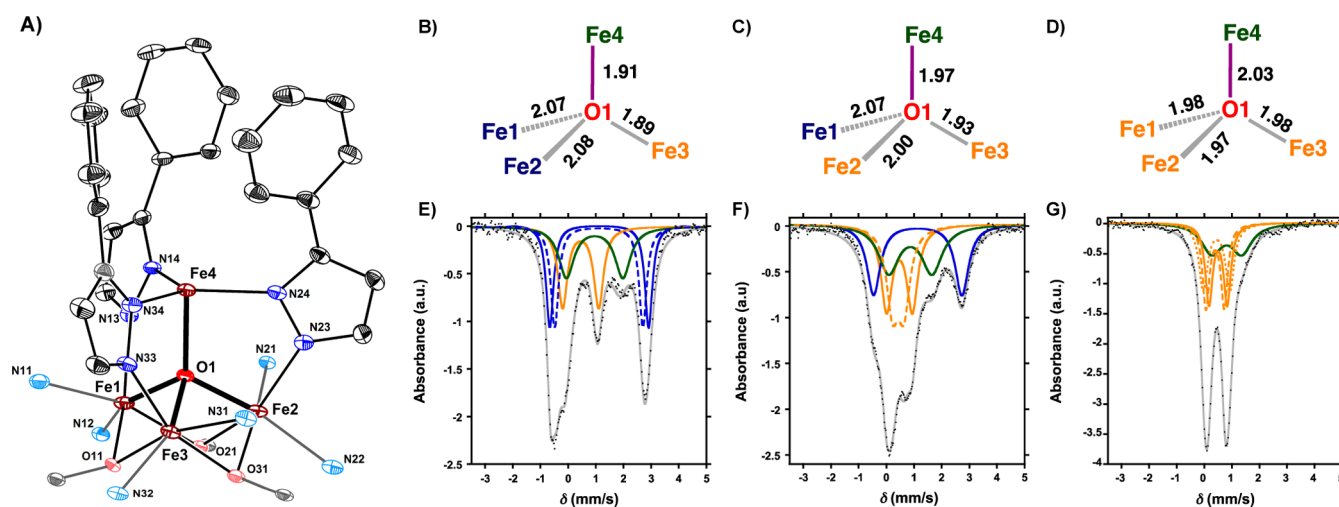


Figure 4. (A) Truncated molecular structure of [LFe₃(PhPz)₃OFe][OTf]₂, with thermal ellipsoids at the 50% probability level. Portions of the ligand (L), hydrogen atoms, outer-sphere counterions, and solvent molecules are not shown for clarity. (B–D) X-ray structural parameters of the [Fe₄(μ₄-O)] core in complexes 3–5. (E–G) Zero-field ⁵⁷Fe Mössbauer spectra at 80 K of (E) [LFe₃(PhPz)₃OFe][OTf] (black dots) with simulated parameters: (i) $\delta = 0.472$ mm/s, $|\Delta E_Q| = 1.188$ mm/s (solid orange trace); (ii) $\delta = 1.121$ mm/s, $|\Delta E_Q| = 3.172$ mm/s (dashed blue trace); (iii) $\delta = 1.128$ mm/s, $|\Delta E_Q| = 3.569$ mm/s (solid blue trace); and (iv) $\delta = 0.953$ mm/s, $|\Delta E_Q| = 2.074$ mm/s (solid green trace). (F) [LFe₃(PhPz)₃OFe][OTf]₂ (black dots) with simulated parameters: (i) $\delta = 0.431$ mm/s, $|\Delta E_Q| = 0.413$ mm/s (dashed orange trace); (ii) $\delta = 0.475$ mm/s, $|\Delta E_Q| = 0.927$ mm/s (solid orange trace); (iii) $\delta = 1.138$ mm/s, $|\Delta E_Q| = 3.190$ mm/s (solid blue trace); and (iv) $\delta = 0.859$ mm/s, $|\Delta E_Q| = 1.563$ mm/s (solid green trace). (G) [LFe₃(PhPz)₃OFe][OTf]₃ (black dots) with simulated parameters: (i) $\delta = 0.394$ mm/s, $|\Delta E_Q| = 0.667$ mm/s (dashed orange trace); (ii) $\delta = 0.442$ mm/s, $|\Delta E_Q| = 0.966$ mm/s (dotted orange trace); (iii) $\delta = 0.501$ mm/s, $|\Delta E_Q| = 0.662$ mm/s (solid orange trace); and (iv) $\delta = 0.811$ mm/s, $|\Delta E_Q| = 1.089$ mm/s (solid green trace). The gray line is a spectral fit of the data.

with a splitting of $|\Delta E_Q|$ of 0.413 mm/s (Figure 2F, dashed orange trace). This shift is consistent with the oxidation from Fe^{II} to Fe^{III}.^{12b} An analogous shift is observed when oxidizing complex 4 to 5 with AgOTf, where three nearly identical quadrupole doublets at $\delta = 0.394$, 0.442, and 0.501 mm/s are

now present (Figure 2F, orange traces). Note that throughout the different oxidation states of the metal cluster the quadrupole doublet at $\sim \delta = 0.859$ mm/s (green trace) remains virtually unchanged, indicating that electron transfer occurs primarily at the triiron core. Such localized redox

Table 2. Mössbauer Parameters for Complexes 3–5

no.	complex	parameters		
		δ (mm/s)	$ \Delta E_Q $ (mm/s)	%
3	[LFe ₃ (PhPz) ₃ OFe][OTf]	0.472	1.188	32
		1.121	3.172	25
		1.128	3.569	21
		0.953	2.074	32
4	[LFe ₃ (PhPz) ₃ OFe][OTf] ₂	0.431	0.413	26
		0.475	0.927	26
		1.138	3.190	26
		0.859	1.563	26
5	[LFe ₃ (PhPz) ₃ OFe][OTf] ₃	0.394	0.667	27
		0.442	0.966	27
		0.501	0.662	27
		0.811	1.089	27

modulation is notable, with the apical metal maintaining the same oxidation state (Fe^{II}) between -2.5 and 1.0 V (vs Fc/Fc⁺). This behavior is attributed to a greater propensity of the core Fe centers to be oxidized, due to the presence of electron-rich alkoxide donors and higher coordination number. This localization of the electron transfer provides a conduit for storing electrons or holes without changing the oxidation state of the metal center that has a coordination site available for substrate binding.

However, the localized oxidation states of the metal clusters might be the results of XRD and Mössbauer measurements being performed at low temperatures (100 and 80 K). In order to determine if the oxidation states remain localized at higher

temperatures, we have performed additional variable-temperature (VT) XRD (100 and 298 K), Mössbauer (80, 100, 200, and 298 K), and NMR (203–293 K) studies, with complex 3 as a representative example (Figures S12–S16 and Tables S1–S3). The X-ray structure at 298 K is very similar to that at 100 K (Figure S12). The Fe1–O1, Fe2–O1, and Fe3–O1 distances change from 2.082(3), 2.102(3), and 1.889(3) (Å) at 100 K to 2.048(2), 2.068(2), and 1.954(3) (Å) at room temperature, respectively, whereas the Fe4–O1 bond distance remains virtually unchanged (Table S2). These results indicate that even at room temperature the oxidation states remain localized to the triiron core. However, some delocalization cannot be excluded, as some variations in the bond distances are present.

The VT zero-field ⁵⁷Fe Mössbauer spectra recorded at 80, 100, 200 K support these findings (Figures S13 and S14 and Table S3). The Mössbauer spectrum of 3 collected at 80 K is similar to that of the analogous triflate salt and shows four quadrupole doublets, consistent with three high-spin Fe^{II} centers and a single high-spin Fe^{III} center.²⁵ Increasing the temperature from 80 to 293 K shows the expected loss of signal intensity due to the temperature dependence of the Lamb–Mössbauer factor.²⁵ Simulating each data set in the same fashion as the 80 K spectrum reveals only minor changes in isomer shift and quadrupole splitting for each isolated Fe center (Figure S14). The observed temperature dependence of the isomer shifts, which tend to decrease with increasing temperature, is consistent with the magnitude of the second-order Doppler shift expected for metal complexes (~ 0.1 mm/s).²⁵ A visual inspection of the data shows that the simulated quadrupole splitting narrows as the temperature increases.

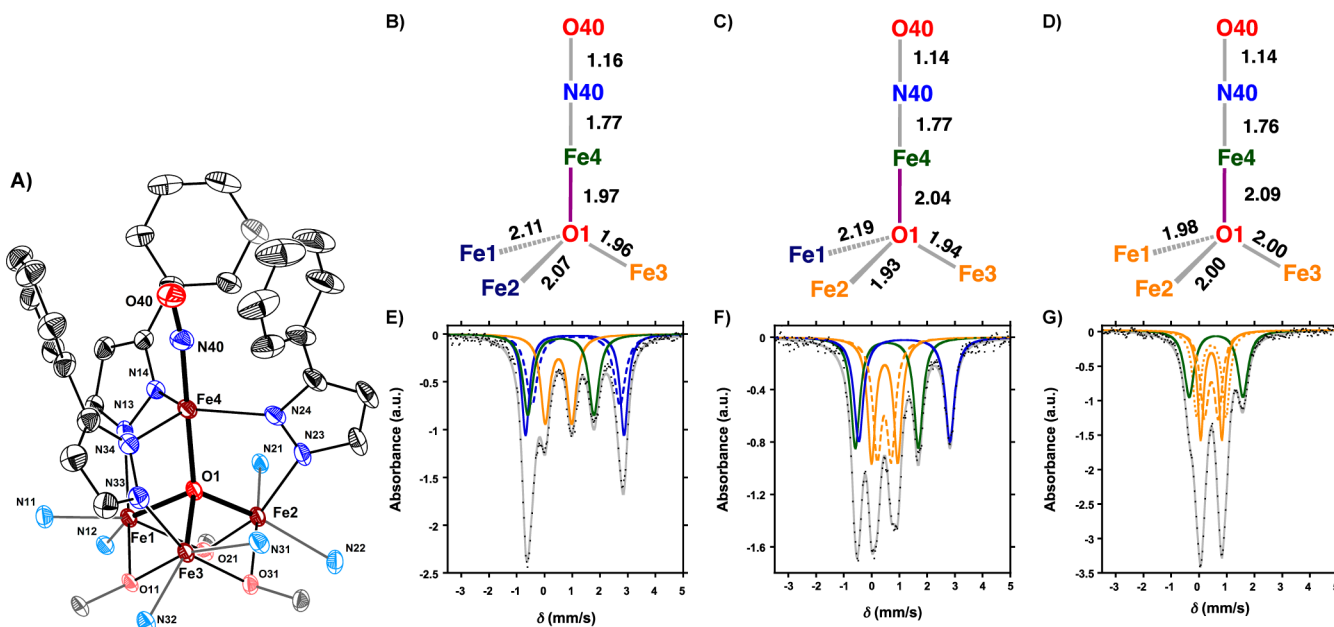


Figure 5. (A) Truncated molecular structure of [LFe₃(PhPz)₃OFeNO][OTf]₂, with thermal ellipsoids at the 50% probability level. Portions of the ligand (L), hydrogen atoms, outer-sphere counterions, and solvent molecules are not shown for clarity. (B–D) X-ray structural parameters of the [Fe₄(μ₄-O)NO] core in complexes 6–8. (E–G) Zero-field ⁵⁷Fe Mössbauer spectra at 80 K of (E) [LFe₃(PhPz)₃OFeNO][OTf] (black dots) with simulated parameters: (i) $\delta = 0.506$ mm/s, $|\Delta E_Q| = 0.956$ mm/s (solid orange trace); (ii) $\delta = 1.094$ mm/s, $|\Delta E_Q| = 3.549$ mm/s (solid blue trace); (iii) $\delta = 1.132$ mm/s, $|\Delta E_Q| = 3.171$ mm/s (dashed blue trace); and (iv) $\delta = 0.592$ mm/s, $|\Delta E_Q| = 2.381$ mm/s (solid green trace). (F) [LFe₃(PhPz)₃OFeNO][OTf]₂ (black dots) with simulated parameters: (i) $\delta = 0.454$ mm/s, $|\Delta E_Q| = 0.504$ mm/s (dashed orange trace); (ii) $\delta = 0.470$ mm/s, $|\Delta E_Q| = 0.945$ mm/s (solid orange trace); (iii) $\delta = 1.177$ mm/s, $|\Delta E_Q| = 3.286$ mm/s (solid blue trace); and (iv) $\delta = 0.550$ mm/s, $|\Delta E_Q| = 2.271$ mm/s (solid green trace). (G) [LFe₃(PhPz)₃OFeNO][OTf]₃ (black dots) with simulated parameters: (i) $\delta = 0.445$ mm/s, $|\Delta E_Q| = 0.509$ mm/s (solid orange trace); (ii) $\delta = 0.445$ mm/s, $|\Delta E_Q| = 0.765$ mm/s (dashed orange trace); (iii) $\delta = 0.445$ mm/s, $|\Delta E_Q| = 1.052$ mm/s (dotted orange trace); and (iv) $\delta = 0.617$ mm/s, $|\Delta E_Q| = 1.937$ mm/s (solid green trace). The gray line is a spectral fit of the data.

The observed temperature dependence of quadrupole splitting is attributed to a Boltzmann population of nearly degenerate electronic states.²⁵ Nevertheless, the room-temperature Mössbauer data features four well-resolved resonances, consistent with the localization of Fe^{II} and Fe^{III} character in the triiron core (Table S3).

The VT-NMR spectra recorded between 203 and 293 K demonstrate a linear correlation between the chemical shifts and the inverse temperature (Figures S15 and S16). The linear correlations in complex 3 exhibit Curie and anti-Curie type behavior between 120 and -20 ppm, which is frequently observed for multimetallic paramagnetic complexes.²⁸ The linear dependence is indicative of the absence of abrupt electronic transitions, which would otherwise alter the exchange interactions between the Fe metal centers and, hence, show a significant deviation from linearity. Consequently our variable-temperature XRD, Mössbauer, and NMR studies all suggest that formal oxidation states in complex 3 remain localized throughout the experimental temperature range.

Utilizing the localized electron transfer in complexes 3–5, we sought to investigate the effect of redox changes on small molecule activation. Nitric oxide (NO) was selected since the ν_{NO} stretch at 1875 cm⁻¹ (gas phase) in the infrared (IR) spectrum is a useful spectroscopic handle²⁹ that is sensitive toward local changes in the electronic environment. NO binding to iron clusters is also of biological significance,³⁰ and the chemistry of NO with synthetic iron–sulfur clusters has been investigated.³¹ Furthermore, the chemistry of NO with various other metal centers is well-established.^{29,32} Notwithstanding, only a handful of iron nitrosyl complexes that feature a trigonal bipyramidal geometry (TBP; Table S4) have been reported.^{16a,d,j,33} A detailed study of the electronic structure of NO adducts of iron dithiolene complexes upon oxidation/reduction of the dithiolene ligand has been reported.³⁴ However, to the best of our knowledge, the effect of redox changes at distal metal centers on the activation of nitric oxide has not been described.

Iron nitrosyl complexes were targeted by treating solutions of 3–5 with NO (Scheme 1). Upon exposure to NO, significant changes are observed in the ¹H NMR spectrum of complexes 3–5 (Scheme 1 and Figures S17–19). These new species were identified by X-ray diffraction studies as the corresponding nitrosyl complexes: [LFe₃(PhPz)₃OFe(NO)][OTf] (6), [LFe₃(PhPz)₃OFe(NO)][OTf]₂ (7), and [LFe₃(PhPz)₃OFe(NO)][OTf]₃ (8) (Figures 5A and S35–S37; *vide infra*). Alternatively, complexes 7 and 8 can be readily synthesized from 6 upon oxidation with 1.0 or 2.0 equiv of AgOTf (Scheme 1).

The electrochemical properties of complex 7 are very similar to those of complex 4. For complex 7, three quasi-reversible redox waves are observed at -1.662, -0.717, and 0.005 V (vs Fc/Fc⁺). These oxidation/reduction waves are assigned to the Fe^{II}₄/Fe^{II}₃Fe^{III} (-1.662 V), Fe^{II}₃Fe^{III}/Fe^{II}₂Fe^{III}₂ (-0.717 V), and Fe^{II}₂Fe^{III}₂/Fe^{II}Fe^{III}₃ (0.005 V) redox couples, respectively.

X-ray diffraction studies on complexes 6–8 (Figures 5A and S35–S37) showed that the coordination environment around the apical iron metal center (Fe4) is trigonal bipyramidal ($\tau_5 = 0.83$ – 0.99).³⁵ The NO and the μ_4 -oxido (O1) are axial with respect to the pyrazolate N14|N24|N34 plane and complete the trigonal bipyramid. For complex 7, the apical iron center is located slightly above the plane formed by pyrazolate nitrogen donors N14, N24, and N34 (Figure 5A). Upon oxidation, a slight increase in distance is observed between the equatorial

plane and Fe4 (6, 0.166 Å vs 8, 0.260 Å). Compared to complexes 3–5, an increase in the (Fe1–N13–N14–Fe4), (Fe2–N23–N24–Fe4), and (Fe3–N33–N34–Fe4) torsion angles is observed in order to facilitate binding of NO (Table 1). The increase in angular torsion results in an average decrease of ~0.12 Å between the Fe1|Fe2|Fe3 and N14|N24|N34 centroids (Table 1). Furthermore, such an increase leads to a decrease in steric crowding around the apical metal center. NO is coordinated in a linear fashion ($\angle\text{Fe–N–O} = 170.9 \pm 1.0^\circ$), consistent with other TBP iron nitrosyl complexes (Table S4). It must be noted that Fe–N–O angle is dependent on the steric crowding around the apical metal center.^{16j}

Similar to complexes 3–5, the μ_4 -oxido (O1) is connected to all four iron centers and forms a rare [Fe₄(μ_4 -O)NO] core (Figure 5B–D).^{17c,18,19} Oxidation of 6 to 8 results in an increase in the Lewis acidity of the triiron core, which, in turn, leads to a decrease in the Fe1|Fe2|Fe3 centroid–O1 distance from 1.057 Å (6) to 0.921 Å (8). Furthermore, oxidation also results in contraction of the Fe1–N13, Fe2–N23, and Fe3–N33 bond distances (Table 1). Other structural changes are found in the [Fe₄(μ_4 -O)NO] core and are dependent on the oxidation state of the iron centers (Table 1). As mentioned above, oxidation from Fe^{II} to Fe^{III} is accompanied by a reduction in bond lengths. For instance, the Fe2–O1 distance changes from 2.070(2) Å in complex 6 to 1.928(3) Å in complex 7 (Figure 5C,D). An even more substantial change is observed for the Fe1–O1 distance upon oxidation from 7 to 8 (7, 2.184(3) Å vs 8, 1.979(5) Å). Correspondingly, in complexes 6–8, electron transfer exclusively occurs from the triiron core as well. The apical iron center can be best described as a {FeNO}⁷ moiety in the Enemark–Feltham notation.³⁶

Complexes that resemble the coordination environment around the apical iron center have been published.^{16a,d,j,33} For instance, Lehnert and co-workers recently published the monometallic complex [Fe(TMG₃tren)(NO)][OTf]₂ (TMG₃tren = 1,1,1-tris{2-[N(2)-(1,1,3,3-tetramethylguanidino)ethyl]-amine}, which features a similar {FeNO}⁷ metal center.^{16d} The average Fe–N_{guan} bond distances (spanning the trigonal plane) of 2.037 Å are nearly identical to those observed in complexes 6–8 (2.077 Å; Table 1). A major difference is the distance between the axial Fe–N_{amine} (2.251 Å) and Fe–O1 (2.035 Å), reflecting the anionic character of μ_4 -oxido (O1). The Fe–N–O angle of 171.4 is similar to that in [Fe(TMG₃tren)(NO)][OTf]₂ (168.0) and is common for sterically encumbered nitrosyl complexes.^{16j} Similar to their structural parameters, the electrochemical properties of [Fe(TMG₃tren)(NO)][OTf]₂ and complexes 6–8 are comparable as well, both of which show a reversible reduction between -1.2 and -1.8 V (vs Fc/Fc⁺). However, chemically, they are different. Whereas treating [Fe(TMG₃tren)(NO)][OTf]₂ with CoCp*₂ results in a clean reduction to a {FeNO}⁸ type complex, treating complex 6 with CoCp*₂ (1.0 equiv) resulted in the formation of complex 3 with concomitant loss of NO (Figures S20 and S21). This process possibly accounts for the asymmetry of the most negative redox wave (-1.662 V vs Fc/Fc⁺) in the CV of complex 6. This is most likely caused by reduction of complex 6 and additional electron transfer to form NO⁻, which is feasible at such low potentials.²⁹

The zero-field ⁵⁷Fe Mössbauer spectra of complexes 6–8 are very similar to those of complexes 3–5 (Figure 5E–G). The change in oxidation state from Fe^{II} to Fe^{III} is readily monitored by a shift of the quadrupole doublets at $\delta \approx 1.1$ mm/s (blue

traces) to a value of $\delta \approx 0.4\text{--}0.5$ mm/s (orange traces). Coordination of NO to the apical iron center lowers the isomer shift to $\delta \approx 0.6$ mm/s in 6–8 (Figure 5E–G, green trace, and Table 3) compared to $\delta \approx 0.8\text{--}0.9$ mm/s in 3–5 (Figure 4E–

Table 3. Mössbauer Parameters for Complexes 6–8

no.	complex	parameters		
		δ (mm/s)	$ \Delta E_Q $ (mm/s)	%
6	$[\text{LFe}_3(\text{PhPz})_3\text{OFeNO}][\text{OTf}]$	0.506	0.956	25
		1.094	3.549	25
		1.132	3.171	25
		0.592	2.381	25
7	$[\text{LFe}_3(\text{PhPz})_3\text{OFeNO}][\text{OTf}]_2$	0.470	0.945	25
		0.454	0.504	25
		1.177	3.286	25
		0.550	2.271	25
8	$[\text{LFe}_3(\text{PhPz})_3\text{OFeNO}][\text{OTf}]_3$	0.445	0.509	27
		0.445	1.052	27
		0.445	0.765	27
		0.617	1.937	27

G, green trace, and Table 2). Mössbauer data for other trigonal bipyramidal iron nitrosyl complexes are summarized in Table S4. The fact that the isomer shift for Fe4 remains relatively unchanged for complexes 6–8 is consistent with XRD data indicating that the oxidation state of the apical metal center does not change during the redox transformations of the iron metal cluster, even upon coordination of NO.

With iron nitrosyl complexes 6–8 in hand, we used infrared (IR) spectroscopy to investigate the effect of distal metal oxidation state changes on the bound NO ligand. The solid-state infrared spectra of complexes 2–8 are shown in Figures S9, S22–25, and 6. Complex 6 exhibits two peaks at 1715 and

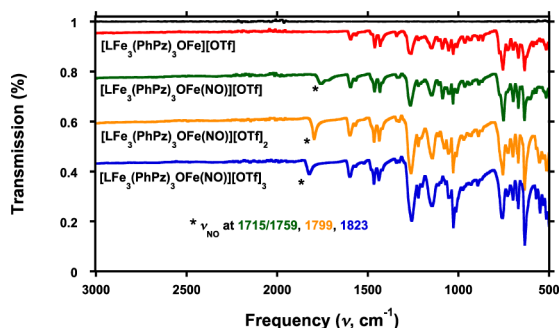


Figure 6. Infrared (IR) spectrum of $[\text{LFe}_3(\text{PhPz})_3\text{OFe}][\text{OTf}]$ (3; red line), $[\text{LFe}_3(\text{PhPz})_3\text{OFeNO}][\text{OTf}]$ (6; green line), $[\text{LFe}_3(\text{PhPz})_3\text{OFeNO}][\text{OTf}]_2$ (7; orange line), and $[\text{LFe}_3(\text{PhPz})_3\text{OFeNO}][\text{OTf}]_3$ (8; blue line). The black line is the baseline.

1759 cm^{-1} , assigned to the NO stretching modes. The presence of two NO bands is unexpected and might be due to Fermi resonances. To investigate further, we prepared the ^{15}NO labeled analogue of complex 6. Isotopic labeling should discern whether the two ν_{NO} stretches are attributed to Fermi resonances or due to the presence of two isomers of complex 6. In the latter case, two ν_{NO} stretches should persist upon isotopic labeling, albeit downshifted. The IR spectrum of the ^{15}NO labeled analogue clearly shows two downshifted ν_{NO} stretches at 1688 and 1726 cm^{-1} (Figure S26; calcd, 1683 and

1727 cm^{-1} , respectively). These studies thus indicate that, most likely, two different geometries of complex 6 are present in the solid state, giving rise to the two observed ν_{NO} stretches in complex 6. However, XRD studies did not unequivocally demonstrate the presence of multiple conformations. Nonetheless, multiple peaks assigned to NO stretches have been observed in other complexes bearing a single NO ligand.^{33d} In contrast, complexes 7 and 8 exhibit single IR bands at 1799 and 1823 cm^{-1} , respectively (Figure 6). The observed NO stretching frequencies are in line with other reported iron nitrosyl complexes in trigonal bipyramidal geometry.^{16a,d,j,33} On average, for complexes 6–8, the ν_{NO} changes by ~ 30 cm^{-1} per one-electron oxidation. Similar changes in ν_{NO} (35 $\text{cm}^{-1}/\text{e}^-$) are observed for a series NO adducts of monoiron dithiolene complexes upon oxidation/reduction.^{34b} In that case, the nature of the ligands coordinated to Fe is significantly affected due to modifications in the redox state of the dithiolene moiety. The significant ν_{NO} shift in the current system is notable, given that neither the oxidation state of the metal binding NO nor the direct donors to the apical Fe is changing. Although purely electrostatic effects on the ν_{NO} stretching frequency cannot be ruled out, analysis of the structural parameters of the clusters provides an alternate explanation for the observed trend.

The most notable and significant change in the bond distance occurs between the apical metal and the interstitial oxygen (O1). Successive oxidation from 6 to 8 leads to an increase of Fe4–O1 bond length from $1.968(2)$ Å in 6 to $2.087(5)$ Å in 8 (Δ Fe4–O1 = 0.119 Å). The decreased interaction between O1 and Fe4 upon oxidation of the triiron core results in lower electron donation to Fe4 and consequently a more electron-deficient metal center. For complexes 6–8, the following trend is thus observed: the more electron deficient the apical metal center, the higher the ν_{NO} stretching frequency. Such a trend was also demonstrated in monometallic complexes of the type $[\text{Fe}(\text{BMPA-pr})][\text{X}]$ (BMPA = *N*-propanoate-*N,N*-bis(2-pyridylmethyl)amine; X = Cl^- , ClO_4^- , I^- , and CF_3SO_3^-).³⁷ In these complexes, a notable shift of 84 cm^{-1} was observed as a function of the coordinating ability of the counterions. Less coordinating counterions, and hence more electron-deficient metal centers, showed higher ν_{NO} stretching frequencies. The large shift of the ν_{NO} frequency was attributed to an increase in π -donation from the NO ligand upon increasing the electron deficiency of the iron metal center, as demonstrated by a linear correlation between the $\nu(\text{Fe–NO})$ and $\nu(\text{N–O})$ stretching frequencies. These results were corroborated by computational studies, describing the Fe–NO interactions as Fe(III) with NO^- , and indicated π -donation from NO^- into the iron $\beta\text{-d}_{xz}$ and $\beta\text{-d}_{yz}$ orbitals upon increasing the electropositive character of the iron metal center.

Given that the observed trends in complexes 6–8 are similar to and that our results fit the above-mentioned report, a mechanism akin to that proposed by Lehnert and co-workers might be operating. Consequently, we attribute the change in ν_{NO} to the flexibility of the axial interstitial oxygen ion (O1), which moves closer to the metal centers that are being oxidized and away from the apical metal that binds the diatomic molecule. The resulting increase in electron deficiency of the apical metal center (Fe4) results in an increase in the π -donation from NO and hence an increase in ν_{NO} , which was observed experimentally. Furthermore, the importance of axial ligand flexibility has also been invoked in mononuclear iron models of the FeMoco cluster of nitrogenase, where the degree of elongation between the axial atom (Si, B, C) of tripodal

supporting ligands was speculated to affect the degree of N_2 and CO activation.³⁸

To exploit the different degrees of NO activation, we investigated the reactivity of the most oxidized and most reduced nitrosyl complexes, **6** and **8**. The addition of complex **6** in dichloromethane to a solution of complex **8** results in the formation of complex **7** upon mixing, as judged by 1H NMR (Figure S27), whereas no dimerization was observed. To further test the chemical reactivity of nitrosyl complexes **6** and **8**, we investigated their reaction with O_2 . Metal–nitrosyl complexes are known to react with O_2 to form NO_2^- .³⁹ The addition of 1 atm of O_2 to complex **6** in dichloromethane (J-Young NMR tube) resulted in clean oxidation **6** within 2 h to give a 1H NMR spectrum that is identical to that of complex **7**. After 24 h, some decomposition was observed (Figure S28). In contrast, no oxidation events were observed for complex **8** upon addition of 1 atm of O_2 (J-Young NMR tube). In both cases, the nitrosyl moieties remained intact (Figures S28 and S29). These studies thus indicate that electron transfer is the predominant observed reactivity pathway.

In our attempts to utilize the reducing power of complex **6**, we investigated the disproportionation of NO. Others have investigated the disproportionation of NO by various metal–nitrosyl complexes as well.^{39c,40} Addition of 6 equiv of NO to complex **6** in acetonitrile resulted in a color change from red-brown to dark green during the course of 28 h. All of the volatiles of the reaction mixture were vacuum-transferred and subsequently trapped by a series of traps at -78 °C (CH_3CN) and -196 °C (all other gases) to allow for analysis of the gaseous products. Fourier transform infrared (FTIR) spectroscopy of the trapped gases revealed clear formation of N_2O , although some NO remained present (Figure 7, blue trace). In

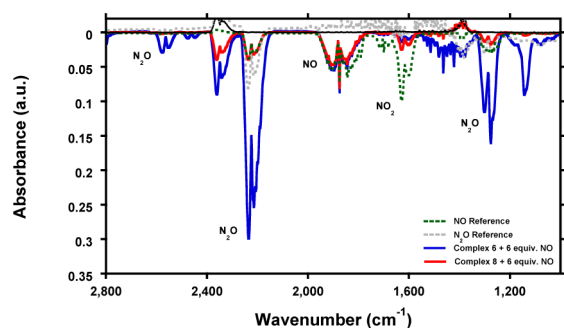


Figure 7. Fourier transform infrared (FTIR) spectrum of NO gas (green trace), N_2O gas (gray trace), and the gaseous volatiles of the reaction of complex **6** (blue trace) and complex **8** (red trace) with 6 equiv of NO.

addition, 1H NMR analysis of the remaining solid revealed quantitative conversion of complex **6** to a species with a 1H NMR spectrum identical to that of complex **7** (Figure S30). However, the fate of the generated NO_2^- could not be determined. In contrast, addition of 6 equiv of NO to complex **8** did not lead to any oxidation (Figure S31), and only a small N_2O peak was observed in the IR spectrum (Figure 7, red trace), which might be due to the small N_2O impurity in the used NO gas (Figure 7, green trace). The green and red traces in Figure 7 are nearly identical, supporting the notion that the observed N_2O is from the N_2O impurity of the NO gas.

These experiments clearly demonstrate the differences in reactivity between complexes **6** and **8**. It is interesting that the

electrons stored in the triiron core of complex **6** can be used to facilitate NO disproportionation at a distal metal center. With the electron reservoir depleted, disproportionation of NO to N_2O is not observed in complex **8**. These results are in line with previous work, where NO disproportionation is favored by electron-rich metal centers.⁴⁰ Overall, the present studies demonstrate that within a cluster with an interstitial oxygen atom the apical Fe–O interaction is flexible and is significantly affected by remote redox changes, which, in turn, affects the activation of the coordinated NO, all of which are aspects relevant to small molecule activation by metal clusters.

SUMMARY

A new class of tetranuclear iron clusters of the general formula $[LFe_3(PhPz)_3OFe][OTf]_x$ ($x = 0, 1, 2,$ or 3) has been synthesized. These clusters feature a discrete $[Fe_4(\mu_4-O)]$ core, which is rare. Additionally, these clusters are site-differentiated, with a triiron core consisting of six-coordinate metal centers and one four-coordinate apical metal. Electrochemical, spectroscopic, and crystallographic studies have demonstrated that upon redox chemistry the triiron core shuttles between oxidation states: $[Fe^{II}_3] \rightleftharpoons [Fe^{II}_2Fe^{III}] \rightleftharpoons [Fe^{II}Fe^{III}_2] \rightleftharpoons [Fe^{III}_3]$. During these redox processes spanning a large potential window, the oxidation state of the apical iron center (Fe4) does not change. The site-specific redox chemistry is due to differences in coordination numbers and the type of ligand. This localization of the redox processes offers a conduit for storing electrons or holes away from the site of substrate binding. Exposure of redox series 3–5 to nitric oxide (NO) yielded the corresponding nitrosyl complexes 6–8. We found that the NO stretching frequency varies by as much as 100 cm^{-1} over three oxidation states of the triiron core. The degree of NO activation was linked to the flexibility of the interstitial oxygen atom (O1), whose ability to donate electron density to the apical iron center is affected by the oxidation state of the triiron moiety. This study shows that the redox changes of metal centers can influence the degree of activation of small molecules on a distal site. These effects occur even in the absence of any redox events at the metal center that directly binds the substrate.

EXPERIMENTAL SECTION

General Procedures. All reactions were performed at room temperature in a N_2 -filled M. Braun Glovebox or by using standard Schlenk techniques unless otherwise specified. Glassware was oven-dried at 140 °C for at least 2 h prior to use and allowed to cool under vacuum. All reagents were used as received unless otherwise stated. Iodosobenzene (PhIO) and $LFe_3(OAc)_3$ were synthesized according to published procedures.^{12b,41} **Caution!** Iodosobenzene is potentially explosive and should be used only in small quantities. Nitric oxide (NO), phenyl-1*H*-pyrazole, $Na(N(SiMe_3)_2)$, AgOTf, and $Fe(OTf)_2$ were purchased from Sigma-Aldrich and Strem Chemicals. Cobaltocene ($CoCp_2$) and decamethyl cobaltocene ($CoCp^*_2$) were purchased from Strem Chemicals and sublimed before use. Anhydrous tetrahydrofuran (THF) was purchased from Aldrich in 18 L Pure-Pac containers. Anhydrous CH_2Cl_2 , diethyl ether, hexane, and THF were purified by sparging with nitrogen for 15 min and then passing under nitrogen pressure through a column of activated A2 alumina. Anhydrous 1,2-dimethoxyethane (DME) was dried over sodium/benzophenone and vacuum-transferred onto molecular sieves. The 1H , ^{19}F , and $^{13}C\{^1H\}$ NMR spectra were recorded at 400.13 and 100.62 MHz on a Bruker Ascend 400 MHz spectrometer equipped with prodigy cryoprobe or at 300.13, 282.36, and 75.47 MHz, respectively, on a Varian 300 MHz spectrometer. All chemical shifts (δ) are reported in ppm, and coupling constants (J) are in hertz. The 1H and $^{13}C\{^1H\}$ NMR spectra

were referenced using residual H impurity in deuterated solvent, whereas the ^{19}F chemical shifts are reported relative to the internal lock signal. CD_2Cl_2 , CD_3CN , and ^{15}N labeled nitric oxide (^{15}NO) were purchased from Cambridge Isotope Laboratories. Deuterated solvents were dried over calcium hydride, degassed by three freeze–pump–thaw cycles, and vacuum-transferred prior to use. The UV–vis spectra were recorded on a Varian Cary Bio 50 spectrophotometer. Infrared (ATR-IR) spectra of complexes 3–8 were recorded on a Bruker APLHA ATR-IR spectrometer at 2 cm^{-1} resolution. Fourier transform infrared (FTIR) spectra of gases were recorded in a sealed IR-Cell using a Bio-Rad Excalibur FTS 3000 spectrometer. Elemental analyses were performed by Robertson Microлит Laboratories.

Physical Methods. Mössbauer Measurements. Zero-field ^{57}Fe Mössbauer spectra were recorded at 80, 100, 200, or 298 K in constant acceleration mode on a spectrometer from See Co (Edina, MN) equipped with an SVT-400 cryostat (Janis, Wilmington, WA). The quoted isomer shifts are relative to the centroid of the spectrum of a α -Fe foil at room temperature. Samples were prepared by grinding polycrystalline material (20 mg) into a fine powder and pressed into a homogeneous pellet with boron nitride in a cup fitted with a screw cap. The data were fitted to Lorentzian lineshapes using the program WMOSS (www.wmooss.org).

Electrochemical Measurements. CVs were recorded with a Pine Instrument Company AFCBP1 bipotentiostat using the AfterMath software package. All measurements were performed in a three-electrode cell configuration that consisted of (1) a glassy-carbon ($\phi = 3.0\text{ mm}$) working electrode, (2) a Pt wire as the counter electrode, and (3) an Ag wire as the reference electrode. All electrochemical measurements were performed at RT in an M. Braun N_2 -filled glovebox with O_2 and H_2O levels $<2\text{ ppm}$. Dry dichloromethane that contained $0.1\text{ M } n\text{Bu}_4\text{NPF}_6$ was used as the electrolyte solution. The ferrocene/ferrocenium (Fc/Fc^+) redox couple was used as an internal standard for all measurements.

X-ray Crystallography. Low-temperature (100 K) and room-temperature (298 K) X-ray data were obtained on a Bruker PHOTON100 CMOS based diffractometer (microfocus sealed X-ray tube, $\text{Mo K}\alpha$ ($\lambda = 0.71073\text{ \AA}$) or $\text{Cu K}\alpha$ ($\lambda = 1.54178$)). All diffractometer manipulations, including data collection, integration, and scaling, were carried out using the Bruker APEXII software.⁴² Absorption corrections were applied using SADABS.⁴³ Structures were solved by direct methods using XS⁴⁴ (incorporated into SHELXTL) and refined by full-matrix least-squares on F^2 . All non-hydrogen atoms were refined using anisotropic displacement parameters. Hydrogen atoms were placed in the idealized positions and refined using a riding model. The structures were refined (weighed least-squares refinement on F^2) to convergence.

Due to the size of the compounds (3–8), most crystals included solvent-accessible voids, which tended to contain disordered solvent. In most cases, this disorder could be modeled satisfactorily. However, for complexes 5 and 8, a significant amount of disorder was found for the solvent and the triflate counterions. The total amount of triflates was fixed at 3, in accordance with the observed bond distances in 5 and 8 and in accordance with other spectroscopic observations. Furthermore, the long-range order of these crystals and amount of high angle data were, in some cases, not ideal due to desolvation of the crystals and/or solvent disorder. These disordered solvent molecules were largely responsible for the alerts generated by the checkCIF protocol.

Synthetic Procedures. Sodium 3-Phenylpyrazolate. In the glovebox, a solution of sodium hexamethyldisilazane (NaHMDS , 3.82 g, 20.8 mmol) in THF (5 mL) was added dropwise to a solution of 3-phenyl-1H-pyrazole (2.50 g, 17.3 mmol) in THF (50 mL). The solution changed from colorless to light yellow upon addition. The homogeneous mixture was stirred for 2 h. The amount of solvent was reduced to approximately 5 mL under vacuum, and hexanes (15 mL) were added until a white precipitate formed. The precipitate was collected by filtration through a sintered glass funnel, washed twice with hexanes (15 mL), and dried under reduced pressure to yield 2.57 g (86%) of sodium 3-phenylpyrazolate (NaPhPz) as a white powder. $^1\text{H NMR}$ (400 MHz, CD_3CN) δ 7.80–7.74 (m, 2H), 7.56 (t, $J = 1.3$

Hz, 1H), 7.30–7.23 (m, 2H), 7.15–7.07 (m, 1H), 6.46 (t, $J = 1.3\text{ Hz}$, 1H). $^{13}\text{C NMR}$ (101 MHz, acetonitrile- d_3) δ 152.12 (Pz NCCH), 141.11 (Pz CHCHN), 138.49 (*i*-Ar), 129.19 (*o*-Ar CH), 125.87 (*m*-Ar CH), 125.77 (*p*-Ar CH), 100.73 (Pz NCCH).

$[\text{LFe}_3(\text{OAc})(\text{OTf})_2]$. In the glovebox, to a slurry of $\text{LFe}_3(\text{OAc})_3$ (500 mg, 0.416 mmol) in CH_2Cl_2 (10 mL) was added methyl triflate (MeOTf , 137 μL , 1.25 mmol). The color changed from orange to yellow, and the mixture became homogeneous within 5 min. The solution was stirred for 30 min, and the solvent was evaporated under reduced pressure to yield $[\text{LFe}_3(\text{OAc})(\text{OTf})_2]$ as a yellow powder (600 mg; 98%). $^1\text{H NMR}$ (300 MHz, CD_2Cl_2) δ 100.68 (s), 85.82 (s), 76.59 (s), 46.94 (s), 44.30 (s), 37.19 (s), 33.75 (s), 30.83 (s), 25.95 (s), 10.46 (s), –4.46 (s). $^{19}\text{F NMR}$ (282 MHz, CD_2Cl_2) δ –47.23. UV–vis (CH_2Cl_2) [ϵ ($\text{M}^{-1}\text{ cm}^{-1}$)]: 250 nm (7.2×10^4), 380 nm (3.0×10^3). Anal. Calcd For $\text{C}_{60}\text{H}_{39}\text{F}_9\text{Fe}_3\text{N}_6\text{O}_{12}\text{S}_3$ [$[\text{LFe}_3(\text{OTf})_3]$]: C, 49.00; H, 2.67; N, 5.71. Found: C, 48.38; H, 2.84; N, 5.17

$[\text{LFe}_3(\text{PhPz})_3\text{OFe}][\text{OTf}]_2$. In the glovebox, a suspension of $\text{LFe}_3(\text{OAc})(\text{OTf})_2$ (1380 mg, 1.0 mmol) in THF (30 mL) was frozen in a cold well. To the thawing suspension was added NaPhPz (550 mg, 3.3 mmol) in THF (5 mL). The color changed immediately to orange, and the suspension became homogeneous during the course of 1 h. The solution was stirred for a total of 2 h, after which iodobenzene (PhIO , 228 mg, 1.0 mmol) was added as a suspension in THF (5 mL). The solution changed to orange-brown immediately and became homogeneous after 0.5 h. The solution was stirred for 1 h, and a brown precipitate formed. To the suspension was added $\text{Fe}(\text{OTf})_2$ (710 mg, 2.0 mmol) as a suspension in THF (5 mL). The suspension was stirred for 24 h and subsequently filtered over a bed of Celite (0.5 cm) on a medium porosity glass frit. The remaining brown solid was dissolved in acetonitrile and filtered, and the solvent was removed under reduced pressure to yield $[\text{LFe}_3(\text{PhPz})_3\text{OFe}][\text{OTf}]_2$ as a brown solid. Yield 750 mg (41%). $^1\text{H NMR}$ (300 MHz, CD_2Cl_2) δ 119.06 (s), 70.91 (s), 68.39 (s), 53.05 (s), 49.65 (s), 43.88 (s), 43.43 (s), 18.25 (s), 15.67 (s), 14.53 (s), 13.02 (s), 6.96 (s), 6.07 (s), 4.92 (s), 4.25 (s), 0.28 (s), –3.65 (s). $^{19}\text{F NMR}$ (282 MHz, CD_2Cl_2) δ –77.64. UV–vis (CH_2Cl_2) [ϵ ($\text{M}^{-1}\text{ cm}^{-1}$)]: 245 nm (11.1×10^4), 443 nm (7.9×10^3). Anal. Calcd (%) for $\text{C}_{86}\text{H}_{60}\text{F}_6\text{Fe}_4\text{N}_{12}\text{O}_{10}\text{S}_2$: C, 56.66; H, 3.32; N, 9.22. Found: C, 56.32; H, 3.32; N, 8.96.

$[\text{LFe}_3(\text{PhPz})_3\text{OFe}][\text{OTf}]$. In the glovebox, to a rapidly stirred solution of $[\text{LFe}_3(\text{PhPz})_3\text{OFe}][\text{OTf}]_2$ (911 mg, 0.5 mmol) in CH_2Cl_2 (20 mL) was added dropwise a solution of cobaltocene (CoCp_2 ; 97 mg, 0.5 mmol) in CH_2Cl_2 (5 mL). The brown solution immediately changed color to red-purple. The solution was stirred for a further 2 h, and the solvent was removed under reduced pressure. The solid was washed with a copious amount of dimethoxyethane (DME; 75 mL) to remove any cobaltocenium triflate. The remaining solid was dissolved in 50 mL of CH_2Cl_2 and filtered over a bed of Celite (0.5 cm) on a medium porosity glass frit. The solvent was removed under reduced pressure to yield $[\text{LFe}_3(\text{PhPz})_3\text{OFe}][\text{OTf}]$ as a red-purple solid. Yield 631 mg (75%). $^1\text{H NMR}$ (300 MHz, CD_2Cl_2) δ 97.34 (s), 60.35 (s), 56.46 (s), 37.46 (s), 34.75 (s), 33.71 (s), 30.25 (s), 24.41 (s), 17.45 (s), 15.21 (s), 13.36 (s), 12.96 (s), 9.74 (s), 8.03 (s), 4.54 (s), 4.31 (s), –3.89 (s), –7.94 (s). $^{19}\text{F NMR}$ (282 MHz, CD_2Cl_2) δ –78.72. UV–vis (CH_2Cl_2) [ϵ ($\text{M}^{-1}\text{ cm}^{-1}$)]: 252 nm (12.3×10^4), 346 nm (7.1×10^4), 509 nm (4.7×10^3). Anal. Calcd (%) for $\text{C}_{85}\text{H}_{60}\text{F}_3\text{Fe}_4\text{N}_{12}\text{O}_7\text{S}$: C, 60.99; H, 3.61; N, 10.04. Found: C, 60.77; H, 3.45; N, 9.98.

$[\text{LFe}_3(\text{PhPz})_3\text{OFe}][\text{OTf}]_3$. In the glovebox, to a rapidly stirred solution of $[\text{LFe}_3(\text{PhPz})_3\text{OFe}][\text{OTf}]_2$ (911 mg, 0.5 mmol) in CH_2Cl_2 (20 mL) was added dropwise a solution of silver triflate (AgOTf ; 130 mg, 0.5 mmol) in CH_2Cl_2 (5 mL). The brown solution slowly changed color to dark purple. The solution was stirred for a further 2 h, and the solvent was removed under reduced pressure. The remaining solid was dissolved in a minimum amount of CH_2Cl_2 ($\sim 15\text{ mL}$) and filtered over a bed of Celite (0.5 cm) on a medium porosity glass frit. The solvent was removed under reduced pressure to yield $[\text{LFe}_3(\text{PhPz})_3\text{OFe}][\text{OTf}]_3$ as a purple solid. Yield 920 mg (93%). $^1\text{H NMR}$ (300 MHz, CD_2Cl_2) δ 167.53 (s), 88.63 (s), 81.04 (s), 78.45 (s), 72.19 (s), 62.91 (s), 45.47 (s), 20.23 (s), 17.85 (s), 17.52 (s), 10.92 (s), 9.04 (s), 6.92 (s), 5.65 (s), 3.00 (s), –2.28 (s), –9.42 (s). $^{19}\text{F NMR}$ (282 MHz, CD_2Cl_2) δ –77.82. UV–vis (CH_2Cl_2) [ϵ (M^{-1}

cm⁻¹): 244 nm (11.4 × 10⁴), 361 nm (7.0 × 10⁴ⁿ⁰), 519 (8.8 × 10³). Anal. Calcd (%) for C₈₅H₆₀F₉Fe₄N₁₂O₁₃S₃: C, 52.99; H, 3.07; N, 8.52. Found: C, 52.15; H, 3.02; N, 8.17.

[LFe₃(PhPz)₃OFe(¹⁴NO)][OTf]. In the glovebox, a 100 mL Schlenk tube was charged with [LFe₃(PhPz)₃OFe][OTf] (501 mg, 0.3 mmol), and CH₂Cl₂ (40 mL) was added. The tube was sealed and degassed by three freeze–pump–thaw cycles on the Schlenk line. While frozen, gaseous nitric oxide (NO, 33 mL, 0.22345 atm, 185.2 mmHg) was added. The mixture was stirred at room temperature for 2 h, during which the color changed from red-purple to red-brown. After 2 h, the solvent was removed under reduced pressure to yield [LFe₃(PhPz)₃OFeNO][OTf] as a dark red-brown solid. Yield 470 mg (92%). ¹H NMR (300 MHz, CD₂Cl₂) δ 105.12 (s), 64.85 (s), 62.21 (s), 58.05 (s), 46.55 (s), 44.63 (s), 39.74 (s), 22.07 (s), 14.04 (s), 14.04 (s), 8.84 (s), 8.06 (s), 6.49 (s), 5.38 (s), 4.34 (s), 3.37 (s), 0.34 (s), -18.13 (s). ¹⁹F NMR (282 MHz, CD₂Cl₂) δ -78.49. UV–vis (CH₂Cl₂) [ε (M⁻¹ cm⁻¹): 249 nm (10.4 × 10⁴), 457 nm (4.3 × 10³). Anal. Calcd for C₈₅H₆₀F₉Fe₄N₁₃O₈S: C, 59.92; H, 3.55; N, 10.69. Found: C, 59.77; H, 4.11; N, 9.74.

[LFe₃(PhPz)₃OFe(¹⁵NO)][OTf]. In the glovebox, a 100 mL Schlenk tube was charged with [LFe₃(PhPz)₃OFe][OTf] (86 mg, 0.052 mmol), and CH₂Cl₂ (10 mL) was added. The tube was sealed and degassed by three freeze–pump–thaw cycles on the Schlenk line. While frozen, gaseous ¹⁵N labeled nitric oxide (¹⁵NO, 234 mL, 0.00548 atm, 4.5 mmHg) was added. The mixture was stirred at room temperature for 2 h, during which the color changed from red-purple to red-brown. After 2h, the solvent was removed under reduced pressure to yield [LFe₃(PhPz)₃OFe(¹⁵NO)][OTf] as a dark red-brown solid. Yield 82 mg (93%). ¹H NMR is identical to that of complex 6.

[LFe₃(PhPz)₃OFe(NO)][OTf]₂. **Method A.** In the glovebox, to a solution of [LFe₃(PhPz)₃OFeNO][OTf] (170 mg, 0.1 mmol) in CH₂Cl₂ (10 mL) was added a solution of silver triflate (AgOTf; 28.5 mg, 0.11 mmol) in CH₂Cl₂ (2 mL). The red-brown solution slowly changed color to dark green. The green solution was stirred for a total of 2 h and filtered over a bed of Celite (0.5 cm) on a medium porosity glass frit. The solvent was removed under reduced pressure to yield [LFe₃(PhPz)₃OFeNO][OTf]₂ as a dark green solid. Yield 156 mg (84%). ¹H NMR (300 MHz, CD₂Cl₂) δ 124.92 (s), 92.96 (s), 76.04 (s), 73.70 (s), 58.35 (s), 55.54 (s), 45.96 (s), 15.34 (s), 13.10 (s), 11.06 (s), 8.75 (s), 6.91 (s), 6.72 (s), 4.24 (s), 2.61 (s), -6.76 (s). ¹⁹F NMR (282 MHz, CD₂Cl₂) δ -78.19. UV–vis (CH₂Cl₂) [ε (M⁻¹ cm⁻¹): 243 nm (12.3 × 10⁴), 426 nm (9.5 × 10³), 650 nm (1.9 × 10³). Anal. Calcd for C₈₆H₆₀F₆Fe₄N₁₃O₁₁S₂: C, 55.74; H, 3.26; N, 9.83. Found: C, 55.92; H, 3.47; N, 9.67.

Method B. In the glovebox, a 100 mL Schlenk tube was charged with [LFe₃(PhPz)₃OFe][OTf]₂ (370 mg, 0.2 mmol), and CH₂Cl₂ (20 mL) was added. The tube was sealed and degassed by three freeze–pump–thaw cycles on the Schlenk line. While frozen, gaseous nitric oxide (NO, 33 mL, 0.17632 atm, 135.0 mmHg) was added. The mixture was stirred at room temperature for 2 h, during which the color changed from yellow-brown to green. After 2 h, the solvent was removed under reduced pressure to yield [LFe₃(PhPz)₃OFeNO][OTf]₂ as a dark green solid. Yield 338 mg (91%). ¹H NMR is identical to that observed for method A.

[LFe₃(PhPz)₃OFe(NO)][OTf]₃. **Method A.** In the glovebox, to a solution of [LFe₃(PhPz)₃OFeNO][OTf] (170 mg, 0.1 mmol) in CH₂Cl₂ (10 mL) was added a solution of silver triflate (AgOTf; 57 mg, 0.21 mmol) in CH₂Cl₂ (2 mL). The solution first changed color from red-brown to dark green and subsequently to dark purple. The dark purple solution was stirred for a total of 2 h and filtered over a bed of Celite (0.5 cm) on a medium porosity glass frit. The solvent was removed under reduced pressure to yield [LFe₃(PhPz)₃OFeNO][OTf]₃ as a dark purple solid. Yield 190 mg (97%). ¹H NMR (300 MHz, CD₂Cl₂) δ 177.15 (s), 141.81 (s), 89.29 (s), 88.78 (s), 82.02 (s), 79.79 (s), 46.97 (s), 17.22 (s), 11.40 (s), 9.86 (s), 4.76 (s), -2.35 (s). ¹⁹F NMR (282 MHz, CD₂Cl₂) δ -77.88. UV–vis (CH₂Cl₂) [ε (M⁻¹ cm⁻¹): 241 nm (11.6 × 10⁴), 503 nm (8.6 × 10³). Anal. Calcd for C₈₅H₆₀F₉Fe₄N₁₃O₁₄S₃: C, 52.19; H, 3.02; N, 9.10. Found: C, 51.11; H, 3.35; N, 8.42.

Method B. In the glovebox, a 100 mL Schlenk tube was charged with [LFe₃(phpz)₃OFe][OTf]₃ (195 mg, 0.1 mmol), and CH₂Cl₂ (20 mL) was added. The tube was sealed and degassed by three freeze–pump–thaw cycles on the Schlenk line. While frozen, gaseous nitric oxide (NO, 33 mL, 0.08816 atm, 67.5 mmHg) was added. The mixture was stirred at room temperature for 2 h, during which the color changed from dark purple to red-brown. After 2 h, the solvent was removed under reduced pressure to yield [LFe₃(PhPz)₃OFeNO][OTf]₂ as a dark red-brown solid. Yield 146 mg (73%). ¹H NMR is identical to that observed for method A.

Reaction of [LFe₃(PhPz)₃OFe(NO)][OTf] with CoCp*₂. In the glovebox, to a rapid stirred solution of [LFe₃(PhPz)₃OFeNO][OTf] (20 mg, 0.012 mmol) in THF (3 mL) was added a suspension of decamethyl cobaltocene (CoCp*₂; 5 mg, 0.015 mmol) in THF (1 mL). During the course of 2 h, the color of the solution changed gradually from red-brown to brown. The volatiles were removed under reduced pressure to yield a red-purple solid (18 mg). The ¹H NMR of the crude material in CD₂Cl₂ was identical to that of [LFe₃(PhPz)₃OFe][OTf] in CD₂Cl₂ (see Figure S21 in the Supporting Information).

■ ASSOCIATED CONTENT

● Supporting Information

The Supporting Information is available free of charge on the ACS Publications website at DOI: 10.1021/jacs.5b07397.

Crystallographic data files (CIF, CIF, CIF, CIF, CIF, CIF).

Synthetic procedures for [LFe₃(PhPz)₃OFe] and [LFe₃(PhPz)₃OFe][BF₄]; reactivity studies with complexes 6 and 8; characterization data and crystal structures (Figures S1–S37); refinement data, bond angles and distances, and spectroscopic, Mössbauer, and structural parameters (Tables S1–S6) (PDF).

■ AUTHOR INFORMATION

Corresponding Author

*agapie@caltech.edu

Notes

The authors declare no competing financial interest.

■ ACKNOWLEDGMENTS

This research was supported by the California Institute of Technology and the NIH (R01-GM102687A). T.A. is a Sloan, Dreyfus, and Cottrell fellow. T.A. and G.de.R. are grateful for a Camille & Henry Dreyfus Environmental Chemistry Fellowship. We thank Michael K. Takase and Lawrence M. Henling for assistance with crystallography. In addition, we would like to thank the anonymous referees for providing useful comments and suggestions.

■ REFERENCES

- (1) (a) Hoffman, B. M.; Lukoyanov, D.; Yang, Z.-Y.; Dean, D. R.; Seefeldt, L. C. *Chem. Rev.* **2014**, *114*, 4041. (b) Lubitz, W.; Ogata, H.; Rüdiger, O.; Reijerse, E. *Chem. Rev.* **2014**, *114*, 4081. (c) Solomon, E. I.; Heppner, D. E.; Johnston, E. M.; Ginsbach, J. W.; Cirera, J.; Qayyum, M.; Kieber-Emmons, M. T.; Kjaergaard, C. H.; Hadt, R. G.; Tian, L. *Chem. Rev.* **2014**, *114*, 3659. (d) Yano, J.; Yachandra, V. *Chem. Rev.* **2014**, *114*, 4175. (e) Fontecilla-Camps, J. C.; Amara, P.; Cavazza, C.; Nicolet, Y.; Volbeda, A. *Nature* **2009**, *460*, 814. (f) Ragsdale, S. W. *Chem. Rev.* **2006**, *106*, 3317. (g) Holm, R. H.; Kennepohl, P.; Solomon, E. I. *Chem. Rev.* **1996**, *96*, 2239.
- (2) McEvoy, J. P.; Brudvig, G. W. *Chem. Rev.* **2006**, *106*, 4455.
- (3) (a) Suga, M.; Akita, F.; Hirata, K.; Ueno, G.; Murakami, H.; Nakajima, Y.; Shimizu, T.; Yamashita, K.; Yamamoto, M.; Ago, H.; Shen, J.-R. *Nature* **2015**, *517*, 99. (b) Umena, Y.; Kawakami, K.; Shen,

- J.-R.; Kamiya, N. *Nature* **2011**, *473*, 55. (c) Ferreira, K. N.; Iverson, T. M.; Maghlaoui, K.; Barber, J.; Iwata, S. *Science* **2004**, *303*, 1831.
- (4) Kok, B.; Forbush, B.; McGloin, M. *Photochem. Photobiol.* **1970**, *11*, 457.
- (5) (a) Nicolet, Y.; Piras, C.; Legrand, P.; Hatchikian, C. E.; Fontecilla-Camps, J. C. *Structure* **1999**, *7*, 13. (b) Volbeda, A.; Charon, M.-H.; Piras, C.; Hatchikian, E. C.; Frey, M.; Fontecilla-Camps, J. C. *Nature* **1995**, *373*, 580.
- (6) Dobbek, H.; Svetlitchnyi, V.; Gremer, L.; Huber, R.; Meyer, O. *Science* **2001**, *293*, 1281.
- (7) Hakulinen, N.; Kiiskinen, L.-L.; Kruus, K.; Saloheimo, M.; Paananen, A.; Koivula, A.; Rouvinen, J. *Nat. Struct. Biol.* **2002**, *9*, 601.
- (8) Darnault, C.; Volbeda, A.; Kim, E. J.; Legrand, P.; Vernede, X.; Lindahl, P. A.; Fontecilla-Camps, J. C. *Nat. Struct. Biol.* **2003**, *10*, 271.
- (9) (a) Ferguson-Miller, S.; Babcock, G. T. *Chem. Rev.* **1996**, *96*, 2889. (b) Tsukihara, T.; Aoyama, H.; Yamashita, E.; Tomizaki, T.; Yamaguchi, H.; Shinzawa-Itoh, K.; Nakashima, R.; Yaono, R.; Yoshikawa, S. *Science* **1995**, *269*, 1069.
- (10) (a) Hoffman, B. M.; Lukoyanov, D.; Dean, D. R.; Seefeldt, L. C. *Acc. Chem. Res.* **2013**, *46*, 587. (b) Spatzal, T.; Aksoyoglu, M.; Zhang, L.; Andrade, S. L. A.; Schleicher, E.; Weber, S.; Rees, D. C.; Einsle, O. *Science* **2011**, *334*, 940. (c) Hinnemann, B.; Nørskov, J. *Top. Catal.* **2006**, *37*, 55. (d) Eady, R. R. *Coord. Chem. Rev.* **2003**, *237*, 23. (e) Einsle, O.; Tezcan, F. A.; Andrade, S. L. A.; Schmid, B.; Yoshida, M.; Howard, J. B.; Rees, D. C. *Science* **2002**, *297*, 1696. (f) Howard, J. B.; Rees, D. C. *Chem. Rev.* **1996**, *96*, 2965.
- (11) Eady, R. R. *Chem. Rev.* **1996**, *96*, 3013.
- (12) (a) Tsui, E. Y.; Agapie, T. *Proc. Natl. Acad. Sci. U. S. A.* **2013**, *110*, 10084. (b) Herbert, D. E.; Lionetti, D.; Rittle, J.; Agapie, T. *J. Am. Chem. Soc.* **2013**, *135*, 19075. (c) Tsui, E. Y.; Tran, R.; Yano, J.; Agapie, T. *Nat. Chem.* **2013**, *5*, 293.
- (13) (a) Garcia-Bosch, L.; Adam, S. M.; Schaefer, A. W.; Sharma, S. K.; Peterson, R. L.; Solomon, E. I.; Karlin, K. D. *J. Am. Chem. Soc.* **2015**, *137*, 1032. (b) Citek, C.; Lin, B.-L.; Phelps, T. E.; Wasinger, E. C.; Stack, T. D. P. *J. Am. Chem. Soc.* **2014**, *136*, 14405. (c) Kanady, J. S.; Lin, P.-H.; Carsch, K. M.; Nielsen, R. J.; Takase, M. K.; Goddard, W. A.; Agapie, T. *J. Am. Chem. Soc.* **2014**, *136*, 14373. (d) Taguchi, T.; Stone, K. L.; Gupta, R.; Kaiser-Lassalle, B.; Yano, J.; Hendrich, M. P.; Borovik, A. S. *Chem. Sci.* **2014**, *5*, 3064. (e) Liu, T.; DuBois, D. L.; Bullock, R. M. *Nat. Chem.* **2013**, *5*, 228. (f) Zheng, S.; Berto, T. C.; Dahl, E. W.; Hoffman, M. B.; Speelman, A. L.; Lehnert, N. *J. Am. Chem. Soc.* **2013**, *135*, 4902. (g) Camara, J. M.; Rauchfuss, T. B. *Nat. Chem.* **2012**, *4*, 26. (h) Citek, C.; Lyons, C. T.; Wasinger, E. C.; Stack, T. D. P. *Nat. Chem.* **2012**, *4*, 317. (i) Hematian, S.; Siegler, M. A.; Karlin, K. D. *J. Am. Chem. Soc.* **2012**, *134*, 18912. (j) McDonald, A. R.; Van Heuvelen, K. M.; Guo, Y.; Li, F.; Bominaar, E. L.; Münck, E.; Que, L. *Angew. Chem., Int. Ed.* **2012**, *51*, 9132. (k) Kanady, J. S.; Tsui, E. Y.; Day, M. W.; Agapie, T. *Science* **2011**, *333*, 733. (l) Seo, M. S.; Kim, N. H.; Cho, K.-B.; So, J. E.; Park, S. K.; Clemancey, M.; Garcia-Serres, R.; Latour, J.-M.; Shaik, S.; Nam, W. *Chem. Sci.* **2011**, *2*, 1039. (m) Harris, T. D.; Betley, T. A. *J. Am. Chem. Soc.* **2011**, *133*, 13852. (n) Do, L. H.; Hayashi, T.; Moënné-Loccoz, P.; Lippard, S. J. *J. Am. Chem. Soc.* **2010**, *132*, 1273. (o) Xue, G.; De Hont, R.; Münck, E.; Que, L. *Nat. Chem.* **2010**, *2*, 400. (p) Bell, S. R.; Groves, J. T. *J. Am. Chem. Soc.* **2009**, *131*, 9640. (q) Friedle, S.; Kodanko, J. J.; Morys, A. J.; Hayashi, T.; Moënné-Loccoz, P.; Lippard, S. J. *J. Am. Chem. Soc.* **2009**, *131*, 14508. (r) Collman, J. P.; Devaraj, N. K.; Decréau, R. A.; Yang, Y.; Yan, Y.-L.; Ebina, W.; Eberspacher, T. A.; Chidsey, C. E. D. *Science* **2007**, *315*, 1565. (s) Halfen, J. A.; Mahapatra, S.; Wilkinson, E. C.; Kaderli, S.; Young, V. G.; Que, L.; Zuberbühler, A. D.; Tolman, W. B. *Science* **1996**, *271*, 1397.
- (14) Tsui, E. Y.; Kanady, J. S.; Agapie, T. *Inorg. Chem.* **2013**, *52*, 13833.
- (15) (a) Tsui, E. Y.; Kanady, J. S.; Day, M. W.; Agapie, T. *Chem. Commun.* **2011**, *47*, 4189. (b) Tsui, E. Y.; Day, M. W.; Agapie, T. *Angew. Chem., Int. Ed.* **2011**, *50*, 1668.
- (16) (a) Matson, E. M.; Park, Y. J.; Fout, A. R. *J. Am. Chem. Soc.* **2014**, *136*, 17398. (b) Scepaniak, J. J.; Vogel, C. S.; Khusniyarov, M. M.; Heinemann, F. W.; Meyer, K.; Smith, J. M. *Science* **2011**, *331*, 1049. (c) Anderson, J. S.; Rittle, J.; Peters, J. C. *Nature* **2013**, *501*, 84. (d) Speelman, A. L.; Lehnert, N. *Angew. Chem., Int. Ed.* **2013**, *52*, 12283. (e) Bigi, J. P.; Harman, W. H.; Lassalle-Kaiser, B.; Robles, D. M.; Stich, T. A.; Yano, J.; Britt, R. D.; Chang, C. J. *J. Am. Chem. Soc.* **2012**, *134*, 1536. (f) Piro, N. A.; Lichterman, M. F.; Harman, W. H.; Chang, C. J. *J. Am. Chem. Soc.* **2011**, *133*, 2108. (g) Reithofer, M. R.; Schrock, R. R.; Müller, P. *J. Am. Chem. Soc.* **2010**, *132*, 8349. (h) Lee, Y.; Mankad, N. P.; Peters, J. C. *Nat. Chem.* **2010**, *2*, 558. (i) MacBeth, C. E.; Golombek, A. P.; Young, V. G.; Yang, C.; Kuczer, K.; Hendrich, M. P.; Borovik, A. S. *Science* **2000**, *289*, 938. (j) Ray, M.; Golombek, A. P.; Hendrich, M. P.; Yap, G. P. A.; Liable-Sands, L. M.; Rheingold, A. L.; Borovik, A. S. *Inorg. Chem.* **1999**, *38*, 3110. (k) Ray, M.; Golombek, A. P.; Hendrich, M. P.; Young, V. G.; Borovik, A. S. *J. Am. Chem. Soc.* **1996**, *118*, 6084. (l) Kol, M.; Schrock, R. R.; Kempe, R.; Davis, W. M. *J. Am. Chem. Soc.* **1994**, *116*, 4382.
- (17) (a) Cotton, F. A.; Wilkinson, G.; Murillo, C. A.; Bochmann, M. *Advanced Inorganic Chemistry*, 6th ed.; Wiley: New York, 1999. (b) Cotton, F. A.; Murillo, C. A.; Pascual, I. *Inorg. Chem.* **1999**, *38*, 2746. (c) Cotton, F. A.; Daniels, L. M.; Falvello, L. R.; Matonic, J. H.; Murillo, C. A.; Wang, X.; Zhou, H. *Inorg. Chim. Acta* **1997**, *266*, 91.
- (18) Murali, M.; Nayak, S.; Costa, J. S.; Ribas, J.; Mutikainen, I.; Turpeinen, U.; Clémancey, M.; Garcia-Serres, R.; Latour, J.-M.; Gamez, P.; Blondin, G.; Reedijk, J. *Inorg. Chem.* **2010**, *49*, 2427.
- (19) (a) Sutradhar, M.; Roy Barman, T.; Drew, M. G. B.; Rentschler, E. J. *Mol. Struct.* **2013**, *1041*, 44. (b) Sutradhar, M.; Carrella, L. M.; Rentschler, E. J. *Inorg. Chem.* **2012**, *2012*, 4273. (c) Malassa, A.; Schulze, B.; Stein-Schaller, B.; Görls, H.; Weber, B.; Westerhausen, M. *Eur. J. Inorg. Chem.* **2011**, *2011*, 1584. (d) Jian, F.; Xiao, H.; Bai, Z.; Zhao, P. *J. Mater. Chem.* **2006**, *16*, 3746. (e) Cotton, F. A.; Daniels, L. M.; Jordan, G. T., IV; Murillo, C. A.; Pascual, I. *Inorg. Chim. Acta* **2000**, *297*, 6.
- (20) (a) Lee, S. C.; Lo, W.; Holm, R. H. *Chem. Rev.* **2014**, *114*, 3579. (b) Venkateswara Rao, P.; Holm, R. H. *Chem. Rev.* **2004**, *104*, 527.
- (21) (a) Chen, L.; Wang, M.; Gloaguen, F.; Zheng, D.; Zhang, P.; Sun, L. *Chem. - Eur. J.* **2012**, *18*, 13968. (b) Goddard, C. A.; Long, J. R.; Holm, R. H. *Inorg. Chem.* **1996**, *35*, 4347. (c) Cecconi, F.; Ghilardi, C. A.; Midollini, S.; Orlandini, A.; Zanella, P. *J. Chem. Soc., Dalton Trans.* **1987**, 831. (d) Trinh, T.; Teo, B. K.; Ferguson, J. A.; Meyer, T. J.; Dahl, L. F. *J. Am. Chem. Soc.* **1977**, *99*, 408.
- (22) (a) Hernández Sánchez, R.; Zheng, S.-L.; Betley, T. A. *J. Am. Chem. Soc.* **2015**, *137*, 11126. (b) Zhao, Q.; Harris, T. D.; Betley, T. A. *J. Am. Chem. Soc.* **2011**, *133*, 8293. (c) Welch, E. J.; Crawford, N. R. M.; Bergman, R. G.; Long, J. R. *J. Am. Chem. Soc.* **2003**, *125*, 11464.
- (23) Clouston, L. J.; Siedschlag, R. B.; Rudd, P. A.; Planas, N.; Hu, S.; Miller, A. D.; Gagliardi, L.; Lu, C. C. *J. Am. Chem. Soc.* **2013**, *135*, 13142.
- (24) (a) Scarborough, C. C.; Sproules, S.; Weyhermüller, T.; DeBeer, S.; Wieghardt, K. *Inorg. Chem.* **2011**, *50*, 12446. (b) McDaniel, A. M.; Tseng, H.-W.; Damrauer, N. H.; Shores, M. P. *Inorg. Chem.* **2010**, *49*, 7981.
- (25) Gutlich, P.; Eckhard, B.; Trautwein, A. X. *Mössbauer Spectroscopy and Transition Metal Chemistry*; Springer: Berlin, 2011.
- (26) (a) Gouré, E.; Carboni, M.; Dubourdeaux, P.; Clémancey, M.; Balasubramanian, R.; Lebrun, C.; Bayle, P.-A.; Maldivi, P.; Blondin, G.; Latour, J.-M. *Inorg. Chem.* **2014**, *53*, 10060. (b) Lalia-Kantouri, M.; Papadopoulos, Christos, D.; Hatzidimitriou, Antonios, G.; Bakas, T.; Pachini, S. Z. *Angew. Chem.* **2010**, *636*, 531. (c) Singh, A. K.; Jacob, W.; Boudalis, A. K.; Tughages, J.-P.; Mukherjee, R. *Eur. J. Inorg. Chem.* **2008**, *2008*, 2820. (d) Chardon-Noblat, S.; Horner, O.; Chabut, B.; Avenier, F.; Debaecker, N.; Jones, P.; Pécaut, J.; Dubois, L.; Jeandey, C.; Oddou, J.-L.; Deronzier, A.; Latour, J.-M. *Inorg. Chem.* **2004**, *43*, 1638. (e) Schmitt, W.; Anson, C. E.; Pilawa, B.; Powell, A. K. *Z. Anorg. Allg. Chem.* **2002**, *628*, 2443. (f) Reynolds, R. A.; Coucouvanis, D. *Inorg. Chem.* **1998**, *37*, 170.
- (27) Reiff, W. M.; Long, G. J. In *Mössbauer Spectroscopy Applied to Inorganic Chemistry*; Long, G. J., Ed.; Plenum Press: New York, 1984; Vol. 1, p 245.
- (28) Bertini, I.; Luchinat, C.; Rosato, A. *Solution NMR of Paramagnetic Molecules*; Elsevier: Amsterdam, 2001; Vol. 2.

- (29) McCleverty, J. A. *Chem. Rev.* **2004**, *104*, 403.
- (30) (a) Ignarro, L. J. *Nitric Oxide*, 2nd ed.; Academic Press: San Diego, 2010. (b) Wasser, I. M.; de Vries, S.; Moënné-Loccoz, P.; Schröder, I.; Karlin, K. D. *Chem. Rev.* **2002**, *102*, 1201. (c) Möller, J. K. S.; Skibsted, L. H. *Chem. Rev.* **2002**, *102*, 1167. (d) Ignarro, L. J. *J. Physiol. Pharmacol.* **2002**, *53*, 503. (e) Culotta, E.; Koshland, D. *Science* **1992**, *258*, 1862.
- (31) (a) Tran, C. T.; Williard, P. G.; Kim, E. *J. Am. Chem. Soc.* **2014**, *136*, 11874. (b) Victor, E.; Lippard, S. J. *Inorg. Chem.* **2014**, *53*, 5311. (c) Harrop, T. C.; Tonzetich, Z. J.; Reisner, E.; Lippard, S. J. *J. Am. Chem. Soc.* **2008**, *130*, 15602. (d) Scott, M. J.; Holm, R. H. *Angew. Chem.* **1993**, *105*, 621.
- (32) (a) Berto, T. C.; Speelman, A. L.; Zheng, S.; Lehnert, N. *Coord. Chem. Rev.* **2013**, *257*, 244. (b) Wright, A. M.; Hayton, T. W. *Comments Inorg. Chem.* **2012**, *33*, 207. (c) Hayton, T. W.; Legzdins, P.; Sharp, W. B. *Chem. Rev.* **2002**, *102*, 935.
- (33) (a) Lu, T.-T.; Chen, C.-H.; Liaw, W.-F. *Chem. - Eur. J.* **2010**, *16*, 8088. (b) Conradie, J.; Quarless, D. A.; Hsu, H.-F.; Harrop, T. C.; Lippard, S. J.; Koch, S. A.; Ghosh, A. *J. Am. Chem. Soc.* **2007**, *129*, 10446. (c) Davies, S. C.; Evans, D. J.; Hughes, D. L.; Konkol, M.; Richards, R. L.; Sanders, J. R.; Sobota, P. J. *Chem. Soc., Dalton Trans.* **2002**, 2473. (d) Hammes, B. S.; Ramos-Maldonado, D.; Yap, G. P. A.; Liable-Sands, L.; Rheingold, A. L.; Young, V. G.; Borovik, A. S. *Inorg. Chem.* **1997**, *36*, 3210. (e) Di Vaira, M.; Ghilardi, C. A.; Sacconi, L. *Inorg. Chem.* **1976**, *15*, 1555. (f) Di Vaira, M.; Tarli, M.; Stoppioni, P.; Sacconi, L. *Cryst. Struct. Commun.* **1975**, *4*, 653.
- (34) (a) Surawatanawong, P.; Sproules, S.; Neese, F.; Wieghardt, K. *Inorg. Chem.* **2011**, *50*, 12064. (b) Ghosh, P.; Stobie, K.; Bill, E.; Bothe, E.; Weyhermüller, T.; Ward, M. D.; McCleverty, J. A.; Wieghardt, K. *Inorg. Chem.* **2007**, *46*, 522. (c) McCleverty, J. A.; Ratcliff, B. J. *Chem. Soc. A* **1970**, 1627. (d) McCleverty, J. A.; Atherton, N. M.; Locke, J.; Wharton, E. J.; Winscom, C. J. *J. Am. Chem. Soc.* **1967**, *89*, 6082.
- (35) Addison, A. W.; Rao, T. N.; Reedijk, J.; van Rijn, J.; Verschoor, G. C. *J. Chem. Soc., Dalton Trans.* **1984**, 1349.
- (36) Enemark, J. H.; Feltham, R. D. *Coord. Chem. Rev.* **1974**, *13*, 339.
- (37) Berto, T. C.; Hoffman, M. B.; Murata, Y.; Landenberger, K. B.; Alp, E. E.; Zhao, J.; Lehnert, N. *J. Am. Chem. Soc.* **2011**, *133*, 16714.
- (38) (a) Creutz, S. E.; Peters, J. C. *J. Am. Chem. Soc.* **2014**, *136*, 1105. (b) Rittle, J.; Peters, J. C. *Proc. Natl. Acad. Sci. U. S. A.* **2013**, *110*, 15898.
- (39) (a) Olabe, J. A. *Dalton Trans.* **2008**, 3633. (b) Roncaroli, F.; Videla, M.; Slep, L. D.; Olabe, J. A. *Coord. Chem. Rev.* **2007**, *251*, 1903. (c) McCleverty, J. A. *Chem. Rev.* **1979**, *79*, 53.
- (40) (a) Franz, K. J.; Lippard, S. J. *J. Am. Chem. Soc.* **1999**, *121*, 10504. (b) Schneider, J. L.; Carrier, S. M.; Ruggiero, C. E.; Young, V. G.; Tolman, W. B. *J. Am. Chem. Soc.* **1998**, *120*, 11408.
- (41) Huang, C.-Y.; Doyle, A. G. *J. Am. Chem. Soc.* **2012**, *134*, 9541.
- (42) APEX-II, Version 2 User Manual, M86-E01078; Bruker Analytical X-ray Systems: Madison, WI, 2006.
- (43) Sheldrick, G. M. SADABS (version 2008/1): Program for Absorption Correction for Data from Area Detector Frames; University of Göttingen: Göttingen, Germany, 2008.
- (44) Sheldrick, G. M. *Acta Crystallogr., Sect. A: Found. Crystallogr.* **2008**, *64*, 112.